UNIVERSITAS BERGENSIS

Medical Physics

Master Thesis

Proton Beam Test

Of A High Granularity Calorimeter For Proton Computed Tomography

---

By: Kristian Austreim

Supervisor: Dieter Röhrich

June 1, 2015

Abstract

Radiation therapy is a non-invasive method of treating cancer. The purpose of it is to stop cancer cells from reproducing properly which will in turn cause the cancer cells to die out. This is achieved by having ionising radiation do enough damage to the DNA molecule in the cells so that they are unable to repair it. This leads to failure in the reproductive phase of the cell cycle and the cell dies. The traditional way to deliver radio therapy is by γ-rays in the form of Bremsstrahlung from an electron accelerator. The radiation is delivered from multiple angles and the beam is normally collimated to fit the projection of the tumour being radiated. The radiation therapy is usually planned according to information gained from CT-scans that map the insides of the patient. X-ray CT provides excellent information about the density distribution of the patient which in turn gives us information about his or her anatomy. This is then used to plan the dose delivery. However, a high-energy photon beam will deposit most of its energy in just up to a few cm of the body and therefore generally delivers a large integral dose to the body during treatment.

Charged particles, like light ions, deliver their dose in a much more convenient fashion than photons. They deposit little energy at the start of their track and deliver more as they slow down, the energy deposition peaks as they come to a halt inside the patient. This energy deposition peak is known as the Bragg Peak. Particle therapy is a branch of radiation therapy that utilises charged particles instead of photons. The advantage of this is that by carefully positioning the Bragg Peak it is possible to deliver a large dose to the tumour while keeping the total dose to healthy tissue at a minimum. It is therefore very important to precisely estimate the range of a particle in a patient to make sure that the desired dose is delivered where it should be.

Regular X-ray CT-scans provide excellent information of how an MeV photon beam will be attenuated by the patient body. This is not quite the case with charged particles as they interact with matter differently from photons. Calculating the stopping power for light ions based on data from X-ray CTs can result in range uncertainties of up to 1 cm. An intuitive way to solve this problem is to use charged particles as the basis for the CT-scan. Using protons, for example, gives us information of the stopping power directly

without the need of conversion from some other modality. A proton-CT device will have to be able to accurately determine the energy and trajectory for each individual proton in order to reconstruct an image. This needs to be done at a rate high enough for it to be suitable in a clinical setting.

One of the proposed concepts for a proton-CT detector is a high-granularity digital sampling calorimeter. Such a prototype has been constructed as a proposed future upgrade in the ALICE experiment. This prototype has been tested at the proton accelerator at KVI in Groeningen, Netherlands and in this thesis we will have a look at how it performs in a therapeutic particle beam. We will look at how the protons scatter as they go through the detector and how the liberated charges collected in the sensitive layers of the detector behave.

Contents

Abstract **iii**

1 Radiation Physics **1**

1.1 Photons Interacting With Matter 1

1.1.1 Photoelectric effect 3

1.1.2 Compton scattering 4

1.1.3 Pair production 4

1.2 Charged Particles Interacting With Matter 5

1.2.1 Energy Loss By Ionisation 5

1.2.2 Coulomb Scattering 7

1.2.3 Radiative Losses 9

1.2.4 Particle Range 9

2 Detector and Calorimetry Physics **11**

2.1 Homogeneous Calorimeters 11

2.2 Sampling Calorimeters 12

2.3 Calorimeter Types 14

2.4 Semiconductor Detectors 15

2.4.1 Energy Band Structure 16

2.4.2 Doping and the PN Junction 16

2.4.3 CMOS and MAPS 17

3 Radiation Therapy **19**

3.1 The Biological Effects of Radiation 19

3.2 Computed Tomography 21

3.3 Radiation therapy with Photons 22

3.4 Particle Therapy 25

4 Proton Computed Tomography **27**

5 Detector characterisation with electron and hadron beams **28**

5.1 PS and SPS experiments 29

5.1.1 Data Acquisition 29

5.1.2 Pedestal Runs 30

5.1.3 Results 30

5.2 Monte Carlo and FLUKA 35

6 KVI Results and Discussion **36**

6.1 Experimental setup 36

6.2 Charge Diffusion in MAPS 39

6.3 Particle Tracks 42

6.4 Pixel Clusters and the Bragg Peak 52

6.5 Range Resolution 60

7 Conclusion **63**

List of Figures

1.1.1 Mass attenuation coefficients for photoelectric (τ), compton (σ), pair production (κ) and total (μ_m) for photons in lead. [5] 2

1.1.2 This figure shows what happens when a photon undergoes photoelectric absorption. The incoming photon is absorbed by an electron which is ejected from the atom. [5] 3

1.2.1 Energy loss by ionisation for different particles in different materials [11]. . 6

1.2.2 The Bragg-peak of a generic charged particle in air. We can see that the ionisation increases as the particle loses energy. [5] 8

2.1.1 Schematic of a sampling calorimeter. [13] 12

2.4.1 Schematic of a pixel in a MAPS detector. [19] 18

3.2.1 Working principles of an X-ray CT machine: The X-ray tube rotates around the patient while a detector array gathers photons on the opposite side. [9] . 22

3.3.1 The illustration shows a medical linac in the treatment room. We can see how the acceleration tube is embedded in the rotating structure and where tthe beam exits through the beam collimator. 23

3.3.2 The illustration shows the dose deposition in water for different particles. It is clear that charged particles are extremely useful when you want to deliver dose to a limited volume. [18] 24

3.4.1 Dose depositions on a tumour and the surrounding tissue for photons (left) and carbon (right). [21] 26

3.4.2 Calibration curves from HU to stopping power. [17] 26

4.0.1 Schematic view of a pCT setup. 27

5.0.1 Basic schematic of the ALICE detector. The proposed position of FoCal is shown in black [3]. 28

5.1.1 Schematic of the prototype setup showing the locations of the P, H, V, F, and B scintillators. 29

5.1.2 Hits map for the whole detector with an EM shower present. It is possible to see which layers have dead channels and chips. 32

5.1.3 Hits distribution from 2 GeV momentum runs at the PS. The black line is from a pedestal run. The big red peak is from particle tracks and the smaller cluster to the right is from EM showers. Plot was provided by Elena Rocco. 33

5.1.4 Filtered hits distribution from the same runs as figure 5.1.3. The black line is from a pedestal run and the smaller cluster to the right is from EM showers. Provided by Elena Rocco. 34

5.1.5 Hits distribution from 250 GeV momentum beam spills. The cluster to the right is from developed EM and hadronic showers. The peak to the left is particle tracks. Everything in between is from partially developed showers. Plot provided by Elena Rocco. 35

6.1.1 3D schematic of the beam line at KVI where we can see the various beam line components [22]. 37

6.1.2 The FoCal equipment on the breadboard in the KVI beam room. We can also see the copper collimators. Between the collimators we can see the aluminium disks we used to adjust beam energy. 38

6.1.3 The FoCal detector seen from the front. We can see the H and V scintillators at the front and the F scintillator behind them. 38

6.2.1 Charge distribution at different incident angles (4.3 degrees in a and 78.1 degrees in b) for the MIMOSA-5 chip (17 μm pitch). The values shown are the average values with a 6 GeV electron beam [15]. 40

6.2.2 a) The number of pixels containing 90% of the freed electrons at different incident angles. b) Most Probable Value of liberated electrons at different angles. MIMOSA-18 chips have 10μm pitch. [15] 40

6.3.1 Path lenght distribution for 122 MeV protons. 43

6.3.2 Path lenght distribution for 170 MeV protons. 44

6.3.3 Path lenght distribution for 190 MeV protons. 45

6.3.4 Distribution of the total scattering angle for 122 MeV protons 46

6.3.5 Distribution of the total scattering angle for 170 MeV protons 46

6.3.6 Distribution of the total scattering angle for 190 MeV protons 47

6.3.7 Scattering angle between layers for 122 MeV protons. 48

6.3.8 Scattering angle between layers for 170 MeV protons. 48

6.3.9 Scattering angle between layers for 190 MeV protons. 49

6.3.10 The curviness (sinuosity) parameter for the path lengths of the three different energies. We can see that the scattering does not matter much in terms of path length. 50

6.3.11 Super position of hits from all layers for a single proton event from KVI. We can see that the proton stays in the same area at about 1 cm x and 0.5 cm y coordinates. 51

6.3.12 Handful of tracks from a 190 MeV run plotted in 3D. 52

6.4.1 Cluster size distribution for the different layers for 122 MeV protons. 53

6.4.2 Cluster size distribution for the different layers for 170 MeV protons 54

6.4.3 Cluster size distribution for the different layers for 190 MeV protons 54

6.4.4 Detector response for 190 MeV protons split between the 4 chips in each layer. Response should be uniform across the chips for the same layers. . . . 56

6.4.5 Detector response for 170 MeV protons split between the 4 chips in each layer. 57

6.4.6 Relationship between estimated energy deposition in each active layer (based on MC) and average number of pixels fired in each layer. 57

6.4.7 Sum of all runs at 122 MeV 58

6.4.8 Sum of all runs at 170 MeV 59

6.4.9 Sum of all runs at 190 MeV. 59

6.5.1 Estimation of Bragg peak position for 122 MeV protons. 61

6.5.2 Estimation of Bragg peak position for 170 MeV protons. 61

6.5.3 Estimation of Bragg peak position for 190 MeV protons 62

List of Tables

1 This table show the relevant parameters for the Bethe-Bloch equation. . . . 7

2 The table shows the measured scattering angles together with estimated angles and relevant variables. 47

1 Radiation Physics

When a particle beam goes through some sort of matter it will gradually lose energy due to the beam particles interacting with the atoms of the target material. For most particles, the main mode of interaction is through the electromagnetic force, but interactions through the strong nuclear force are also possible for higher energies. In this section we will look at the main modes of interaction with matter for both photons and charged particles at energy levels suitable for medical applications.

1.1 Photons Interacting With Matter

The photon is one of the elementary particles and it is the quantum of all electromagnetic radiation, including light. It is electrically neutral and considered to be the force carrier of the electromagnetic force. The neutral charge makes it so that it is impossible for photons to undergo inelastic interactions with atomic electrons [12]. Photons have three main ways to interact with matter: The photoelectric effect, Compton scattering and pair production. The probabilities for each of them happening varies with photon energy and the atomic number of the target material. Figure 1.1.1 shows how the cross sections vary with energy with a fixed Z, in our case, lead. The spikes correspond to increases in the cross section for the photoelectric effect as the photon energy approaches the binding energy for a new electron shell. Compton scattering is the only one where the photon survives. It is scattered of a quasi-free atomic electron and continues in a different trajectory while the electron is given some of its energy as kinetic energy. In the other two options the photon is completely absorbed in the interaction. The nature of these reactions explain two of the main differences between charged particles and photons interacting with matter:

i) X-rays and γ-rays penetrate matter many times more easily than charged particles.

ii) A photon beam does not lose energy as it traverses a medium. When a photon interacts through any of those three modes, it is either absorbed or scattered out of the beam. The result being that the beam degrades in intensity instead [12].

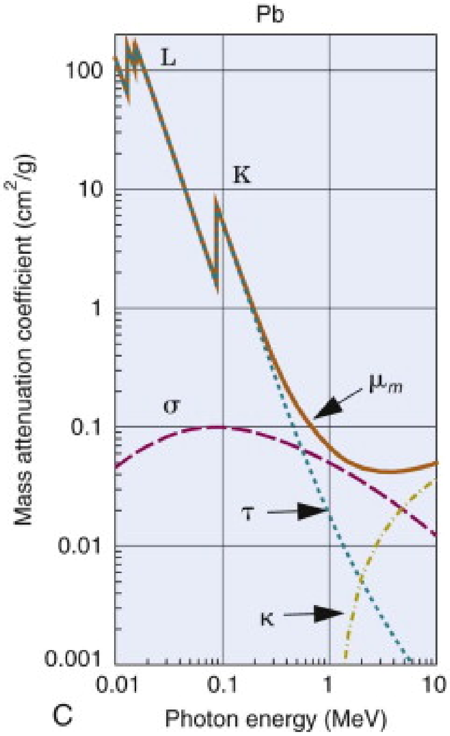

Figure 1.1.1: Mass attenuation coefficients for photoelectric (τ), compton (σ), pair production (κ) and total (μ_m) for photons in lead. [5]

When an ideal photon beam, a monochromatic beam with a small, well defined radiation area, enters a some target the beam intensity is reduced expontentially. It follows the formula

$$I = I_0 e^{-\mu_{tot} x} \tag{1}$$

Where I_0 is the original intensity, μ_{tot} is the attenuation coefficient and x is the depth in the material. μ_{tot} is usually given with units [1/cm], but it is sometimes given as mass attenuation coefficient with units [cm^2/g]. In the latter case x is given as the interaction depth with units [g/cm^2]. μ_{tot} is the algebraic sum of the attenuation coefficients of the different modes of interaction: $\mu_{tot} = \mu_{CS} + \mu_{PE} + \mu_{PP}$. The components are attenuation coefficient for Compton Scattering, Photoelectric Effect and Pair Production respectively.

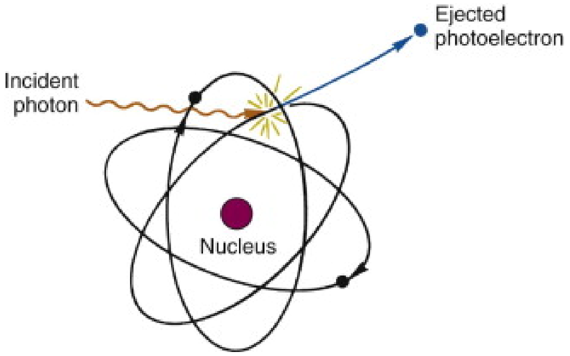

Figure 1.1.2: This figure shows what happens when a photon undergoes photoelectric absorption. The incoming photon is absorbed by an electron which is ejected from the atom. [5]

1.1.1 Photoelectric effect

First we have the photoelectric effect. In this interaction the photon is fully absorbed by the target atom and an electron (referred to as photoelectron) is ejected from the atom. Part of the photon energy is used to free the ejected electron from the atom and the rest is converted to kinetic energy. The photoelectron gains kinetic energy equal to

$$E_e = E_\gamma - E_b \tag{2}$$

Where E_e is the kinetic energy of the photoelectron, E_γ is the incident photon energy, and E_b is the binding energy. Figure 1.1.2 is a simple schematic for the process. The energy deposited in the target body comes from ionisations and excitations caused by the now free electron. When an inner electron is freed from its parent atom, an outer electron can jump in from one of the outer electron shells to fill the vacant space. This releases energy equal to the potential difference between those two shells and is referred to as characteristic X-rays. Furthermore, if this characteristic radiation is absorbed by another electron inside the atom, the electron can be sent out instead. These freed electrons are called Auger electrons. The photoelectric effect is dominant for lower energies and high Z for the absorber material. The Z dependence varies depending on the energy. At the MeV scale, the cross section goes as Z^4 or Z^5. And as can be seen in figure 1.1.1, it decreases drastically as energy increases.

1.1.2 Compton scattering

The second type of interaction is called Compton scattering and it is an elastic collision between a photon and an electron. This happens when the binding energy of the electron is much lower than the photon energy. The electron is then for all practical purposes a free particle and conservation of momentum and energy dictates that it is impossible for the photon to transfer all of its energy to the electron. Taking these conservations in mind it can be shown that the change in the incident photons wave length is $\Delta\lambda = \frac{h}{m_e c}(1 - cos\theta)$ cm. By inserting $E = hc/\lambda$ and $E' = hc/\lambda'$ we get the fractional energy loss for the photon:

$$\frac{E'}{E} = \frac{1}{1 + (E/m_e c^2)(1 - cos\theta)} \tag{3}$$

The probability of a Compton scattering happening does not depend on the atomic number of the absorber material, but every electron can be treated as an independent scattering center. Therefore the cross section is dependent on the density of electrons. The cross section also decreases as the photon energy increases.

1.1.3 Pair production

The third type of interaction is pair production. In this interaction a photon with sufficient energy is transformed to an electron and a positron. When a massless particle annihilates into two massive particles it needs to transfer some momentum to another particle in order to conserve momentum overall. The photon usually interacts with the electric field from a nucleus. The big difference in rest mass between the nucleus and the resulting electron-positron pair means that very little energy is transfered to the nucleus. This effectively makes the lower energy threshold for pair prodction $E_{Thres} = 2m_e c^2 = 1.022MeV$. If the photon interacts with the electric field from an electron the threshold energy becomes $4m_e c^2$. The cross section for Pair Production is approximately proportional to $Z^2 + Z$ for the absorber material. [4].

1.2 Charged Particles Interacting With Matter

Charged particles behave differently when passing through matter than photons do. As a charged particle traverses some medium it will mostly lose its energy due to inelastic collisions with atomic electrons that end up ionized or excited. If the charged particle is a heavy particle (i.e. heavier than electrons) these interactions will only slightly alter the particles path, thus allowing it to make an almost straight path in the target medium. However, it can also undergo elastic interactions with the target nuclei's Coulomb field. These collisions will alter the particles path much more than the inelastic interactions with atomic electrons mentioned earlier. Some other ways a charged particle can lose energy include Čerenkov radiation, Bremsstrahlung and Transition Radiation. The ability of a material to stop an incomming particle beam is called the material's stopping power. It is usually denoted as $\langle -dE/dx \rangle$ with units $[keV/\mu m]$. One can also divide this by the material density to gain the corresponding mass stopping power $-\frac{1}{\rho}\frac{dE}{dx}$. The latter nomination is handy as the stopping power of materials with similar atomic number, Z, is similar when normalized with regard to density. As a result, a particle will have similar energy loss in $1g/cm^2$ of both Iron and Aluminium. Using mass stopping power is also convenient when dealing with compound materials. Radiation Lenght (X_0) is another useful notation. It is defined as the distance an electron moves in a medium before its energy is reduced by a factor $1/e$ from radiative losses only. This notation is useful because if the material thickness is expressed in units of radiation lengths, then the equation for radiative energy loss is simplified to

$$-\left(\frac{dE}{dt}\right) = E_0 \tag{4}$$

where t is the distance in radiation lengths and the calculated energy loss will be basically independent of the absorbing material in question [12]. As with the photons, different processes dominate at different energies as shown in figure 3.

1.2.1 Energy Loss By Ionisation

Ionisation and excitation of atomic electrons is the dominant source of energy loss for heavy particles going through matter. The average energy loss of a particle per unit length is given by the Bethe-Bloch equation (Equation 5).

$$\left\langle -\frac{dE}{dx} \right\rangle = Kz^2 \frac{Z}{A} \frac{1}{\beta^2} \left[\frac{1}{2} ln \left(\frac{2m_e c^2 \beta^2 \gamma^2 W_{Max}}{I^2} \right) - \beta^2 - \frac{\delta(\beta\gamma)}{2} \right] \tag{5}$$

[8]

Where W_{Max} is given as

$$W_{Max} = \frac{2m_e c^2 \beta^2 \gamma^2}{1 + 2\gamma \frac{m_e}{M} + \left(\frac{m_e}{M}\right)^2} \tag{6}$$

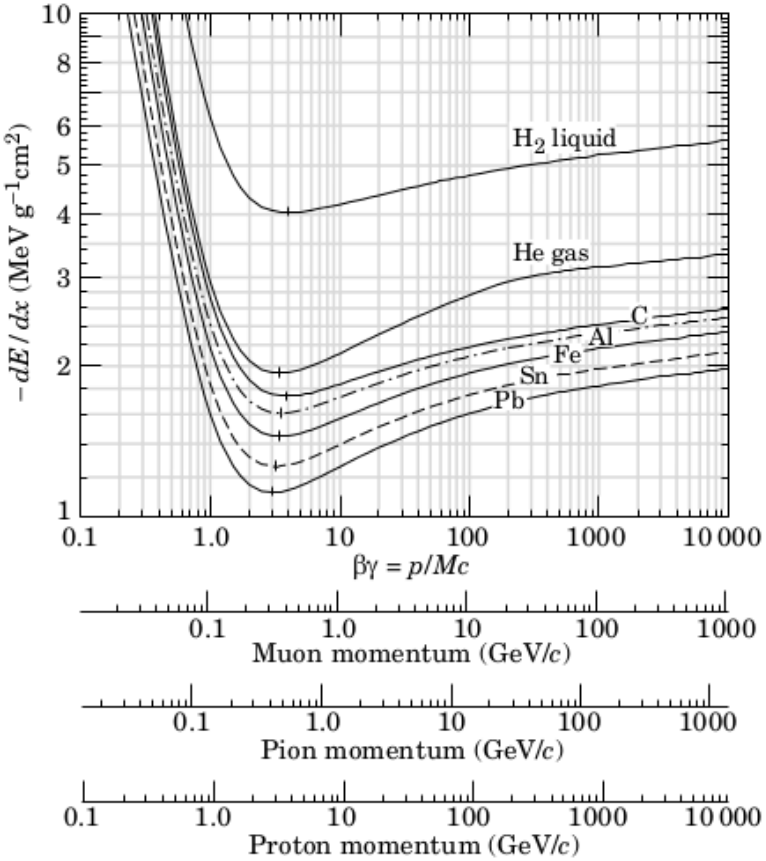

Figure 1.2.1: Energy loss by ionisation for different particles in different materials [11].

Symbol	Definition	Value or units
K	$4\pi N_A r_e^2 m_e c^2$	0.307075 MeV mol^{-1} cm^2
W	Energy transfer to an electron in a single collision	MeV
M	Incident particle mass	MeV/c^2
m_e	Electron mass	$0.511\ \mathrm{MeV}/c^2$
r_e	Classical electron radius	2.818 fm
N_A	Avogadro's number	$6.022 \times 10^{23} mol^{-1}$
A	Atomic mass of absober	g mol^{-1}
I	Mean excitation energy	eV
z	Charge number of incident particle	
Z	Charge number of absorber	
$\delta(\beta\gamma)$	Density effect correction to ionisation energy loss	
β and γ	Usual relativistic meanings	

Table 1: This table show the relevant parameters for the Bethe-Bloch equation.

As can be seen from figure 1.2.1 and equation 5, a charged particle will deposit more energy per unit length as it slows down. This results in having the bulk of the energy deposited in a confined area. This is called a Bragg-peak and is an extremely useful property in medical physics. The Bragg-peak is illustrated in figure 1.2.2.

1.2.2 Coulomb Scattering

When a charged particle goes through matter it can also undergo an interaction called Coulomb Scattering. In this process the projectile particle interacts with the Coulomb field from the absorber nuclei, deflecting it from its original path. To the first order this scattering behaves like Rutherford or Mott scattering, depending on if the projectile is hadronic, and on the spin of the projectile and target nucleus. Especially in thin absorbers where the probability for more than one scattering event is negligible. Rutherford scattering is the simplest of the two as it looks at scattering of spin 0 projectiles on spin 0 target nuclei. The differential cross section, $\frac{d\sigma}{d\Omega}$, for Rutherford Scattering is shown in equation

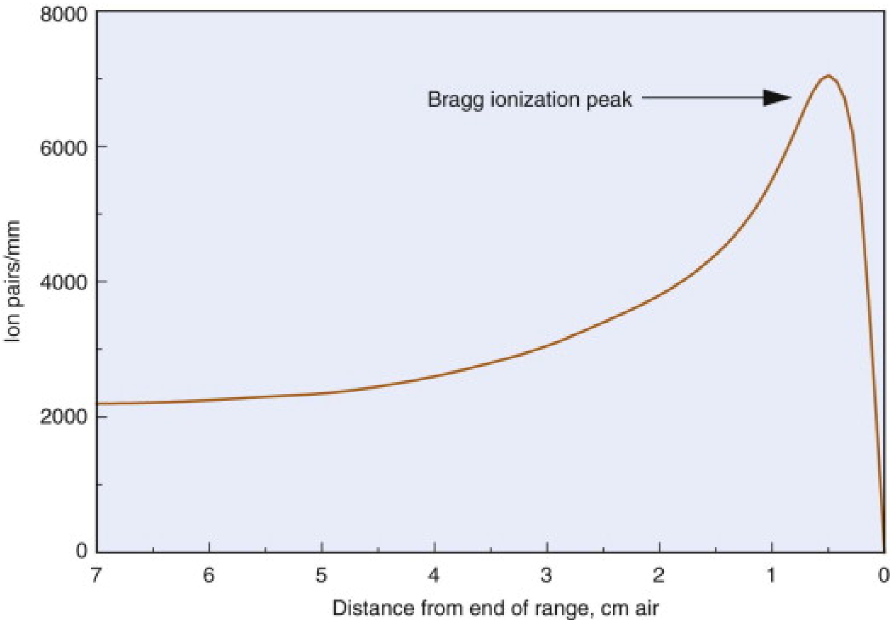

Figure 1.2.2: The Bragg-peak of a generic charged particle in air. We can see that the ionisation increases as the particle loses energy. [5]

7. [11]

$$\left(\frac{d\sigma}{d\Omega}\right)_R = \frac{4m^2(Z_P Z_T e^2)^2}{q^4} \tag{7}$$

Where m is the projectile particle mass, Z_P and Z_T are the charge number of the projectile and target respectively while e is the elementary charge. q is the momentum transfer and is given as

$$q = 2psin(\frac{1}{2}\theta) \tag{8}$$

Given an absorber thick enough that the average number of scattering events exceed 20 [12], while the energy loss remains low, the problem can be treated statistically. The solid angle distribution is approximately Gaussian for small angles. At larger angles the $1/sin^4(\frac{1}{2}\theta)$ dependancy of the scattering takes over and produces a non-Gaussian tail. Experimental and theoretical studies [8] show that the middle 98% of the angular distribution can be adequately approximated with a Gaussian fit around

$$\theta_0 = \theta^{rms}_{plane} = \frac{1}{\sqrt{2}}\theta^{rms}_{space} \tag{9}$$

Where

$$\theta_0 = \frac{13.6MeV}{\beta cp} z \sqrt{\frac{x}{X_0}} \left[1 + 0.038 ln(x/X_0)\right] \tag{10}$$

And p is the momentum, βc the velocity, and z the charge number of the incomming particle. x/X_0 is the material thickness in radiation lengths. θ_0 is gained from making a Gaussian fit to a Moliére radius and the fitting is accurate to 11% in the thickness range $10^{-3} < x/X_0 < 100$.

1.2.3 Radiative Losses

When a particle is deflected it emits electromagnetic radiation. This is called Bremsstrahlung or braking radiation. The energy emitted is proportional to $(E/mc^2)^4$ so this is usually negligible for heavier particles, but one of the main energy loss factors for high-energy electrons and positrons. Bremsstrahlung is also used as the definition of a useful notation called critical energy, E_c, which is the energy at which an electrons energy loss from ionisation is equal to the energy loss from bremsstrahlung [10]. It is only dependent on the material the electron is going through and for solids it can be approximated as

$$E_c = \frac{610MeV}{Z + 1.24} \tag{11}$$

1.2.4 Particle Range

Calculating the range of a charged particle going through matter is an almost impossible task. The randomness of whether or not a particle will undergo an interaction with a very high energy transfer or if it will just undergo gradual energy loss by ionization and Coulomb scattering leads to a large range straggling interval. [10] In principle, it is possible to calculate by integrating over stopping power:

$$R = \int_E^0 \left(-\frac{dE}{dx} \right)^{-1} \mathrm{d}E \tag{12}$$

But as the function for energy loss is dependant on the energy in a complicated matter (different processes dominant at different energies etc) one would usually use an approximation. A common approximation is derived from the Bethe-Bloch formula (equation 5):

$$R \approx \frac{\pi \epsilon_0^2 m_e E^2}{n_A Z_A Z^2 e^4 M} \tag{13}$$

Here it is assumed that the particle energy, E, is much larger than the average ionization energy for the medium and that the incident particle is in the non-relativistic energy range. While this is a relatively crude appoximation, fitting with range curves gives us that the particle range $R \approx E^{1.75}$ which is not too far off [20].

2 Detector and Calorimetry Physics

Some of the main uses for detectors in particle physics include particle tracking, identification and calorimetry. In this chapter we will go through the relevant concepts and workings behind the FoCal prototype. The prototype is a calorimeter made of layers of Si-detectors with tunsten absorbers in between. The silicon layers are Monolithic Active Pixel Sensors (MAPS) made with Complementary Metal Oxide Semiconductor (CMOS) technology.

In principle, every type of particle interaction can be the basis of a particle detector. Meaning that there is a plethora of different particle and radiation detectors. And since different interactions are dominant at different energies, several types of detectors are relevant when examining the properties of a single type of particle. At its core, a detector absorbs part of, or all of, the available energy of the incoming particle and converts it to a measurable signal with some clever mechanic. [10]. The FoCal prototype is an electromagnetic calorimeter, which means that it is designed to absorb and measure energy from electrons and photons. There are two main archetypes of calorimeters: Homogeneous calorimeters and sampling calorimeters.

2.1 Homogeneous Calorimeters

Homogeneous calorimeters are detectors made from a material that functions both as the sensitive part of the detector and the absorbing part. This solution provides a good energy resolution compared to its counterpart as all of the particle energy is deposited in the active part of the detector. This also limits the usefulness of homogeneous calorimeters for particle identification and position measurements as all of the particle energy needs to be absorbed in the same part of the detector to keep the energy resolution. All calorimeter types get contributions to the energy resolution from variations in energy leakage and variations in the initial interaction point. Generally, the energy resolution of a calorimeter

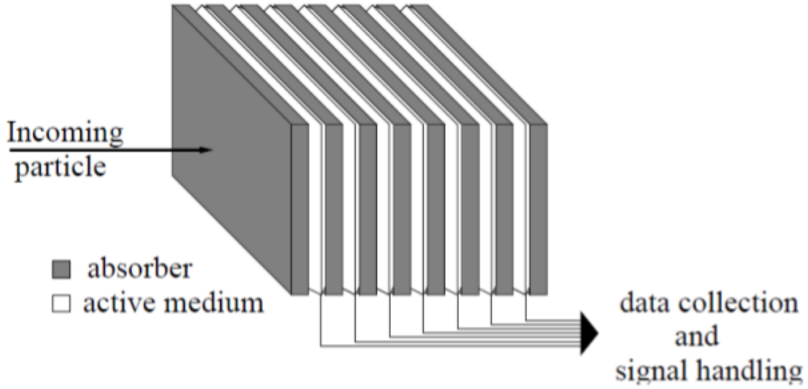

Figure 2.1.1: Schematic of a sampling calorimeter. [13]

can be written as

$$\sigma^2 = \sigma_1^2 + \sigma_r^2 + \sigma_l^2 + \sigma_b^2 \tag{14}$$

Where σ_1 is related to the fluctuations of the first interaction, σ_r and σ_l are rear and lateral leakage while σ_b from leakage due to albedo fluctuations. [10]

2.2 Sampling Calorimeters

Sampling calorimeters consist of alternating layers of passive absorbers and sensitive materials. As a result, only a part of the radiation energy will be picked up by the sensitive components of the detector, which reduces the energy resolution compared to a homogeneous detector. On the other hand, segmentation allows for the collection of information about incident angle and position. Typical absorbers are high-density materials like iron and tungsten which allows for much more compact detectors. The absorbers are also usually much cheaper than the active layers, making the detector more economical overall (if one should choose to prioritise information about position and incident angle over energy resolution). Since each active layer only measures a sample of the deposited energy we get an uncertainty term from the sampling itself. In an ideal situation the relative uncertainty would just be $\sigma_{samp} = 1/\sqrt{N_{Tot}}$, where N_{Tot} is the total number of intersection points and is given by

$$N_{Tot} = \frac{T}{d} \tag{15}$$

With d being the thickness of one detector segment (sensitive layer and absorber) and T is the total track length. T can be estimated as

$$T = \frac{E}{E_c} \cdot X_0 \tag{16}$$

But since the number of detected particles is determined by the detection threshold, the measurable track length is somewhat shorter. It can be approximated as

$$T_m = F(\xi) \cdot \frac{E}{E_c} \cdot X_0 \quad [g/cm^2] \tag{17}$$

Where $F(\xi)$ is a function that corrects for the cutoff parameter on the total measurable tracklength and can be parametrised as

$$F(\xi) = (1 + \xi ln(\frac{\xi}{1.53}))e^{\xi} \tag{18}$$

ξ is a function of the critical energy of the detector and the detection energy threshold (ϵ_{th}) and is given as

$$\xi = 2.29 \cdot \frac{\epsilon_{th}}{E_c} \tag{19}$$

In addition, particle scattering will have an effect on the effective thickness of the detector. If a particle scatters at an angle θ the amount of material it needs to traverse in one layer goes from d to $d/cos(\theta)$. These corrections give us a more realistic value for the number of interaction points:

$$N = F(\xi) \cdot \frac{E}{E_c} \cdot \frac{X_0}{d} \cdot cos(\theta) \tag{20}$$

Using this result we get that the sampling fluctuations have the following contribution to energy resolution [10]:

$$\left[\frac{\sigma(E)}{E}\right]_{Samp} = \sqrt{\frac{E_c \cdot d}{F(\xi) \cdot E \cdot X_0 \cdot cos(\theta)}} \tag{21}$$

The random nature of energy deposition and relatively thin layers in sampling calorimeters can also cause large variations in the amount of energy deposited in each layer. This effect becomes more prominent in thin detector layers and more so in gas-based calorimeters than solid materials. One can approximate the resolution contribution of these Landau fluctuations as

$$\left[\frac{\sigma(E)}{E}\right]_{Landau} \propto \frac{1}{\sqrt{N} \cdot ln(k \cdot \delta)} \tag{22}$$

Where k is a constant and δ is the average energy loss per detector layer. Another factor to consider for the energy resolution is the path length fluctuation of scattered low-energy electrons. Depending on their direction, and the thickness and density of the detector, the energy they deposit in the active layers may vary significantly [1]. Lets call this σ_{Range}. Taking these factors into account we get an expression for the energy resolution of an electromagnetic sampling calorimeter:

$$\left[\frac{\sigma(E)}{E}\right]^2_{Total} = \left[\frac{\sigma(E)}{E}\right]^2_{Sampling} + \left[\frac{\sigma(E)}{E}\right]^2_{Landau} + \left[\frac{\sigma(E)}{E}\right]^2_{Range} \tag{23}$$

2.3 Calorimeter Types

There are several undertypes of calorimeters corresponding to different interactions. Some of these interactions include scintillation photons, ionization and čerenkov radiation [10].

Scintillation detectors are detectors that measure scintillation light. The working principle is that the incoming particle interacts with the atomic electrons of the scintillating material which then releases photons in the form of fluorescence. These photons are then converted to a current by a photodetector. It the material is a plastic the interaction is the excitation of the electrons, while electron-hole pairs are produced in crystals. Popular materials for this kind of detector are crystals like CsI (Cesium Iodide) for homogeneous calorimeters and plastic scintillators for sampling calorimeters.

The čerenkov detectors are similar in the sense that they detect photons generated by the incoming radiation as it traverses the detector. The difference lies in how the photons are generated. Čerenkov radiation are photons (in the blue end of the visible spectrum) emitted from a charged particle as it goes through a transparent medium at a speed higher than the speed of light in that medium. Typical materials used for this include high-density glass and water (used in the Super-Kamiokande experiment). The blue glow one often sees in nuclear reactors is from čerenkov radiation.

Ionisation calorimeters are made from a material where the incoming radiation is able to free electrons from their atoms. An electric field is applied so that the charges are separated and measured. The sensitive material in ionisation detectors can be either gaseous, liquid or solid. Noble gases are popular materials for the gas and liquid based detectors. When the incident radiation ionises an atom, the electron and ion are accelerated towards the anode and cathode, and they may ionise other atoms during this process. The result is a measurable current, and the amplitude of this current is proportional to the energy deposited by the incident radiation. Semiconducting materials are usually the material of choice in solid-state ionisation detectors and since the FoCal prototype is such a detector, we will take a closer look on these.

2.4 Semiconductor Detectors

The basic working principle of a semiconducting detector is analogue that of a gas ionisation detector. In a gas ionisation detector the incomming particle ionises the gas, creating electron-ion pairs. In the semiconductor the medium is a solid and the incomming radiation creates electron-hole pairs instead. The advantage of the semiconductor is that the energy required to generate an electron-hole pair is about one magnitude lower than the energy required to create an electron-ion pair which improves the possible energy resolution. The increased density gives the semiconductor detectors more stopping power, allowing for more compact detectors. They also have very fast response times. However, the disadvantage of using a crystalline solid medium instead of a gas is that it is more suscepible to radiation damage.

Semiconductor materials generally require cooling to low temperatures to be useful as detectors to avoid having too much dark current from thermal electrons jumping to the conducting band. This means that the detectors take up more space due to the necessity of a cryogenic system. Crystalline silicon is one of the semiconducting materials that can be utilised as a detector in room temperature.

2.4.1 Energy Band Structure

Semiconductors are materials whose outer shell atomic levels have an energy band structure. This means that there is an energy gap between the valence band, where the electrons are too bound to the atom to move around in the crystal lattice, and the conducting band, where the electrons can move freely in the semiconductor crystal. The electrons are not able to occupy the energy gap between the bands. The bands are made up of many discrete energy levels that are close enough together to be seen as a continuum while the energy gap is a region where all the energy states are unavailable. The band structure is due to overlapping wavefunctions for the electrons as the atoms are packed closely together in the crystal lattice. From the Pauli principle we have that more than one electron cannot occupy the same energy state. Because of this, the degeneracy in the outer atomic shell energy levels break into the many discrete and closely spaced energy levels that make of the energy bands. This does not affect the inner shell electrons however, as they are more tightly bound to their respective atoms. The width of the energy gap is dependent on the distance between the atoms in the crystal lattice which means that parameters like pressure and temperature have an impact on the performance of the semiconductor detector. [12]

2.4.2 Doping and the PN Junction

The electrical properties of a semiconductor crystal can be altered by so-called doping. Doping is achieved by purposefully adding impurities to the crystal. These impurities are atoms of elements with either more or fewer electrons in the valence band, depending on which properties you want. Silicon, for example, has 4 electrons in its valence band. Doping it with Boron (one less outer electron) would create a p-type semiconductor while doping it with Arsenic (one more electron) would make it an n-type. These doping atoms add either an extra hole or an extra electron to the lattice, increasing the conductivity of the crystal and they are refered to as donors or receptors depending on whether they give an extra electron or take one.

Combining the properties of both p-type and n-type semiconductors in one piece of material creates a so-called PN-junction. This can be accomplished by difusing doping atoms into a doped semiconductor of the opposite type. Both the n-type and the p-type parts of the semiconductor are neutral, but charge carriers will diffuse between the parts due to the excess of electron holes on one side and electrons on the other. The result is a net negative charge on the p-type side and positive charge on the other with a region depleted of free electrons / holes in the middle. This also creates an electric field across this region. The depleted region is the sensitive part of a semiconductor detector. Incoming ionising radiation will excite electrons to the conducting band which will then be accelerated by the E-field while the resulting hole will be filled by other electrons, effectively moving the positive hole the opposite way. This results in a current that can be measured that is also proportional to the ionisation.

2.4.3 CMOS and MAPS

MAPS (Monolithic Active Pixel Sensor) detectors are made using the Complimentary Metal-Oxide-Semiconductor (CMOS) technology. The active layer of a MAPS detector is a lightly doped p-type epitaxial layer that can be as thin as just a few microns. Beneath this layer is the substrate which is made from a highly doped p-type material. N-type and p-type wells are laid on top of the epitaxial layer. Infrastructure like transistors are fitted in the p-type wells as the interface between the light p-type and regular p-type creates a potential well that keeps the electrons in the ligthly doped epitaxial layer. This is also the case for the interface between the epitaxial layer and the substrate. A depleted region will form around the n-type wells, causing electrons to be drawn towards them by the resulting E-field. This is where the electrons liberated by incoming radiation is collected. Advantages of using MAPS detectors include very high detection efficiency and excellent single point resolution. They also have potential to be made very thin to reduce the chance of multiple scattering and can potentially be relatively cheap since they are made with CMOS technology. A disadvantage comes from the fact that the E-field in the depleted regions is heavily localised, so most charge carriers only reach the charge collection diode by thermal diffusion [15]

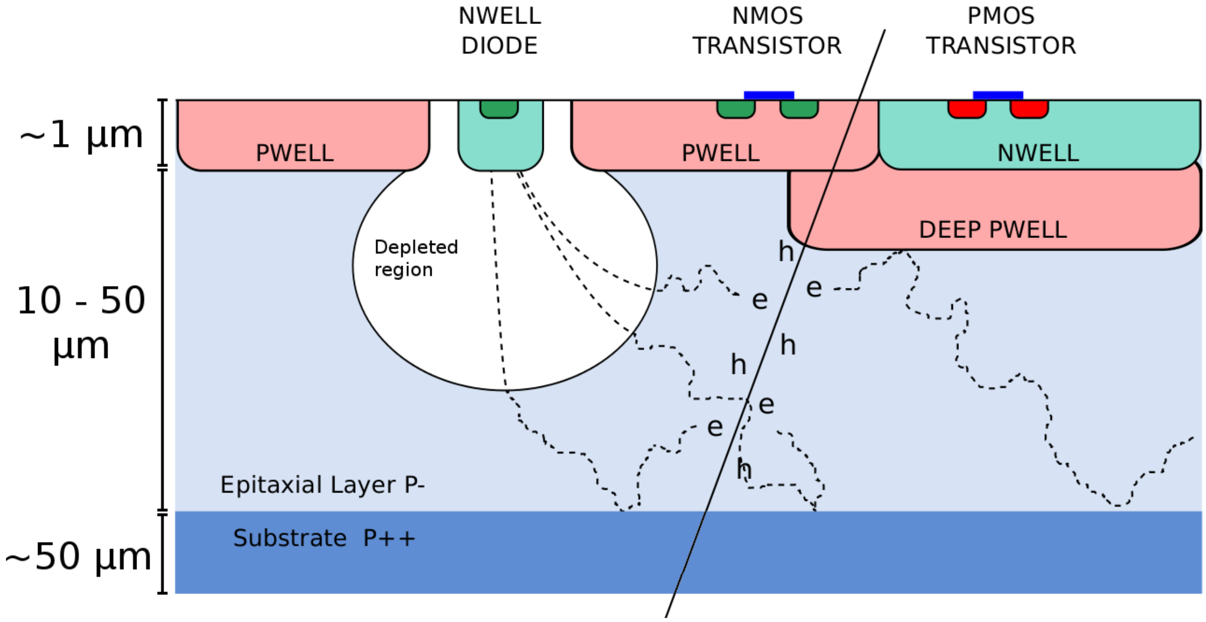

Figure 2.4.1: Schematic of a pixel in a MAPS detector. [19]

3 Radiation Therapy

Cancer is one of the leading causes of deaths in todays society. The term "Cancer" is a broad term encompassing a wide variety of diseases with some common key aspects. Cancer is characterized as a group of abnormal cells undergoing uncontrolled growth. They also have the ability to split of from the main tumour and spread to other parts of the body and form more, secondary tumours. This phenomenon is called metastasis. The three most common methods of cancer treatment is surgery, chemical therapy and radiation therapy. A patient usually undergoes a combination of two or all of these treatments when fighting cancer.

Radiation therapy is a procedure in which the goal is to irradiate a specific volume of the body in order to kill or severely damage the cells in a cancer tumour. The most common way to administer radiation therapy is by utilising MeV-photons from electron linear accelerators, but the use of light ions like protons, helium and carbon has become more popular in recent years. The number of patients receiving radiation therapy increased by about 50% in the period 2001-2010 [14]. So the technology and techniques for radiation treatment is in constant need to evolve to cope with the increased demand while also reducing the chance of complications during treatment. In this chapter we will discuss the basics of radiation treatment and the imaging modalities used to assist with the planning and administration of the treatment.

3.1 The Biological Effects of Radiation

As stated ealier, the point of radiation therapy is to deliver a high enough dose to a defined region in the patients body in order to damage the DNA of the cancer cells. The damage caused by the radiation is determined by the linear energy transfer (LET) of the radiation. This varies between different types of particles and the amount kinetic energy they have. LET is defined as the energy deposited per unit length, and is usually denoted with units [keV/μm]. Particles with LET below $\approx 10keV/\mu m$ are considered to be low-LET particles. Therapeutic photons are categorised as such with an estimated LET of $\approx 0.2 keV/\mu m$. Heavy charged particles are considered as high-LET particles and can have values of $100 - 200 keV/\mu m$ [16]. This does of course vary with energy according to the Bethe-Bloch formula. The LET of a radiation species says something about how densely ionising the radiation is and it is desirable to have high LET in the target volume to maximise the chance of irrepairable DNA damage. The Relative Biological Effect (RBE) has been defined to show the difference in biological effect between different types of radiation when the same dose has been administered. The RBE is given by

$$RBE = \frac{Dose\ of\ reference\ radiation}{Dose\ of\ test\ radiation} \tag{24}$$

250 kVp X-rays or ^{60}Co γ-rays are generally used as reference dose. RBE varies with many factors including, but not limited to, radiation species, type of target tissue, and dose. The RBE factor increases as LET increases untill it reaches the point where it will kill the cell. It is possible for cells to repair the DNA if only one strand of the double helix is broken and higher LET gives a higher chance for a double strand break, which for all intents and purposes kills the cell [16].

The total energy deposited in a material is usually referred to as absorbed dose, D. Dose is defined as the energy deposited per unit mass material has the unit Gray (1 Gy = 1 J/kg). Because LET varies as a particle goes through matter it might be misleading to only use absorbed dose as a measurement of how much damage that has been caused by the radiation. Some types of radiation may also produce secondary radiation, so that the total dose is delivered by different types of radiation. The term Equivalent Dose, denoted H_T, has been coined to help compare the effects of different types of primary radiation. Equivalent dose is given by

$$H_T = \sum W_R \cdot D_R \tag{25}$$

Where H_T is the total equivalent dose, and W_R and D_R are the weighting factors and delivered dose from a specific type of particle. Photons and electrons are considered to have weighting factors of 1 while light ions like helium nuclei have a weighting factor of 20.

Different types of tissue also react differently to radiation damage. The term Effective Dose, denoted as E, has been defined to compare the effectiveness of radiation on different types of tissue. It is given as

$$E = \sum W_T \cdot H_T \tag{26}$$

Here H_T is the equivalent dose given to a specific type of tissue while $W_T$is the weighting factor for that tissue. The effective dose, E, is the sum of all these contributions. It is especially important to take effective dose into consideration when dealing with a region where both "serial" and "parallel" organs will receive radiation. A "serial" organ is an organ which will be rendered useless if one part of it is damaged. The spine is an example of such an organ. "Parallel" organs are able to function even if one part of them is too damaged to work. The liver is an example of such an organ. Both equivalent and effective dose have dimensions [J/kg], but they use the unit Sievert (Sv) to differentiate them from unweighted dose (Gy).

3.2 Computed Tomography

The first ting that needs to be done when a patient is going to receive radiation therapy is to create a treatment plan. A good treatment plan requires good knowledge of the patient's inner anatomy. Information about the tumour location and nearby organs is needed in order to plan a dose field that will do enough damage to the cancer cells while keeping radiation to healthy tissue at a tolerable level and the density distribution is needed to know how the radiation will propagate and deposit energy inside the body. The standard way of getting this information now is by X-ray computed tomography (X-ray CT).

The working principle of X-ray CT is that the X-ray tube rotates around the patient while emitting X-rays that pass through the patient. CT scanners usually operate in the 30-120 keV energy range. They are generated as bremsstrahlung by electrons hitting a target in the X-ray tube. The energy spectrum is therefore continuous with spikes corresponding to the material of the anode in the tube. Some of the X-ray beam is attenuated or scattered in the body while most of it is picked up by a detector on the opposite side. By doing this from all angles around the patient the machinery is able to calculate the attenuation coefficients for voxels of tissue in the patient's body. The attenuation coefficients are then normalised with respect to the attenuation of water. This is quantified in

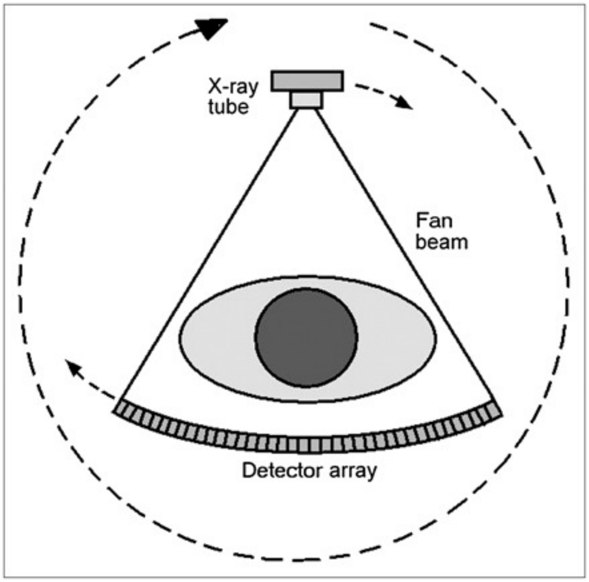

Figure 3.2.1: Working principles of an X-ray CT machine: The X-ray tube rotates around the patient while a detector array gathers photons on the opposite side. [9]

the Hounsfield Unit (HU) which is given by

$$HU = 1000x\frac{\mu_{tissue} - \mu_{water}}{\mu_{water}} \tag{27}$$

and the voxels are put in a grey scale based on this number. By definition, water has HU = 0 while air is -1000 HU. Different parts of the body can range from -1000 HU to +3000 HU.

One of the current limitations of X-ray CT is that it is hard to distinguish between tissue types with similar densities. This can make it hard to figure out where there is a tumour so diagnostic CT images can often be used together with something from another modality.

3.3 Radiation therapy with Photons

Just as X-ray CT is the standard diagnostic imaging modality, the standard radiation treatment modality is using photons. Therapeutic photon beams use energies on the MeV scale up about 25 MeV. Like X-rays, therapeutic photons are also generated from brem-

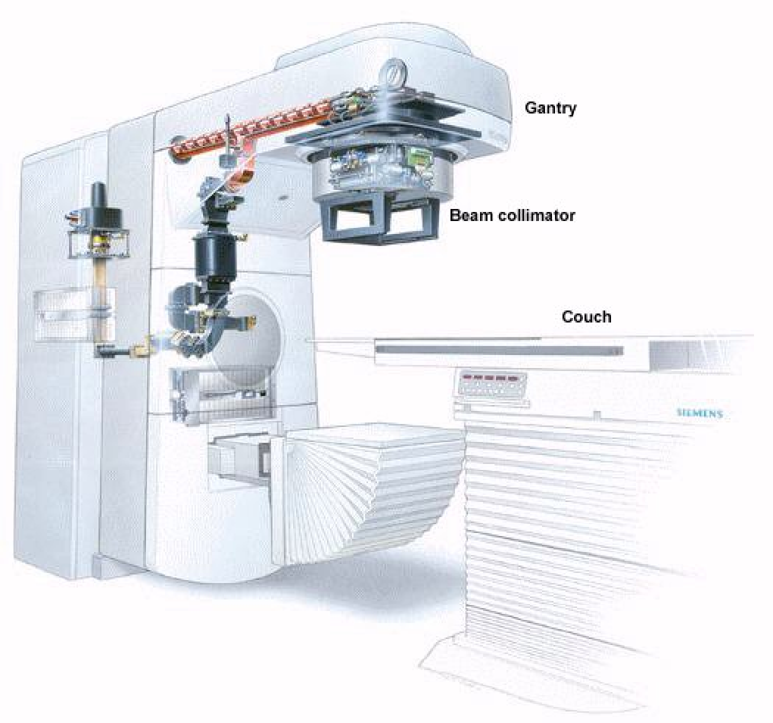

Figure 3.3.1: The illustration shows a medical linac in the treatment room. We can see how the acceleration tube is embedded in the rotating structure and where tthe beam exits through the beam collimator.

strahlung from electrons, but at much higher energies. The beam is produced from a linear accelerator that accelerates electrons up to 25 MeV and then collides them into some material with high Z, like tungsten. Since the photon spectrum from bremsstrahlung is continuous, 25 MeV photons have the maximum energy from a machine with those settings, but most photons have lower energies.

Treatment with photons has been around for a very long time, and many techniques have been developed to improve it in different ways over the years. The addition of adjustable thin collimator leaves allows the radiation field to be shaped like the projection of the target tumour and/or shield sensitive organs close to the target. The beam intensity can also be modulated to suit the 3D shape of the target and surrounding tissue even more. This is accomplished by using flattening filters and wedges in the beam. It is also possible to do these things continuously while the gantry moves around the patient. This maximises the beam directions which will reduce the amount of radiation a given volume

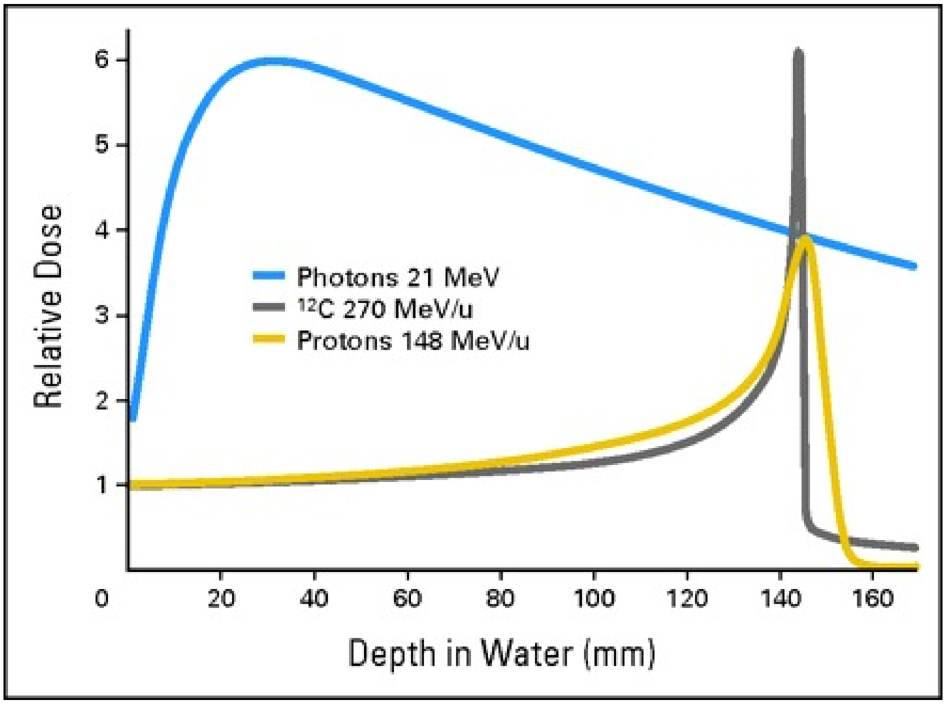

Figure 3.3.2: The illustration shows the dose deposition in water for different particles. It is clear that charged particles are extremely useful when you want to deliver dose to a limited volume. [18]

of healthy tissue receives, while still irradiating the target volume.

These improvements to dose delivery is made possible due to improvements to CT technology. Better images and density distribution data allows for more accurate planning. Even though X-ray CT imaging and photon radiation rely on the same type of particles, different processes dominate the attenuation at the different energy levels. Attenuation of X-rays are dominated by the photoelectric effect, while Compton scattering and pair production dominate in the therapeutical range. A conversion from Hounsfield Units to electron density has to be made to properly map the attenuation of the therapeutical photon beam. The way this is solved now is by making calibration curves based on scanning phantoms with known electron density.

3.4 Particle Therapy

Particle therapy is the treatment of cancer by using charged particles, like protons and light ions, to deal the necessary damage to the target tumour. As shown in figure 3.3.2, a charged particle will deposit most of its energy in a confined space, peaking at the so-called Bragg peak. The main advantages of using charged particles over photons stems from this dose curve. It makes it possible to increase the dose delivered to the tumour while keeping the dose delivered to healthy tissue at acceptable levels. In the long run this will reduce side-effects for patients.

While charged particles have the potential to be superior to photons in terms of effectiveness in killing cancer and preserving healthy tissue, they do have their own complications. It can be argued that 3.3.2 is unfair against photons since it only shows the dose deposition from one beam. The technology to irradiate the patient from virtually any angle is already standard in photon radiation therapy where the accelerator is mounted inside the rotating part. For charged particles there is a completly other story. Even protons need large gantries with powerful magnets in order to rotate the beam line around the patient. Charged particles also require large accelerators in order to achieve the required energies for therapy.

The difference in dose distribution in a patient is shown in figure 3.4.1. Here we can see how much of the healthy tissue that can be spared from being irradiated. On the other hand, having a sharp dose curve requires extremely good precision in order to avoid having the Bragg peak going outside the target volume. In order to be able to predict the position of the Bragg peak one needs information about the stopping power of the target. This information can in principle be gathered from X-ray CT scans. By using a regular CT-scanner on a phantom with known elemental composition one can make a calibration curve connecting the linear attenuation coefficient for X-rays to the stopping power for charged particles since the elemental composition can be used to make a simplified Bethe-Bloch equation to calculate stopping power with. The problem arises when looking at more complicated structures with larger variations in density, like bone and soft tissue. Non-linearities will then cause uncertainties as shown in figure 3.4.2 [17].

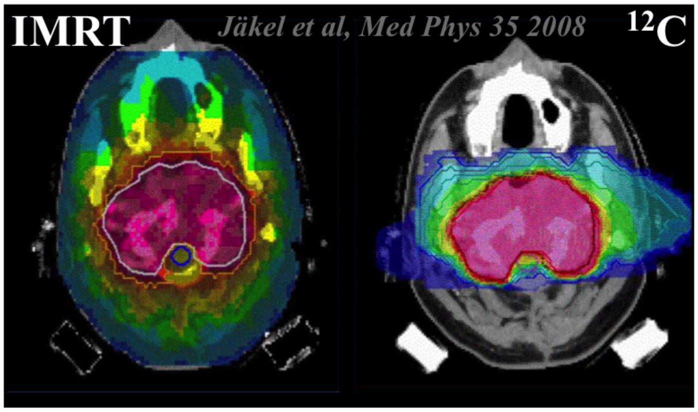

Figure 3.4.1: Dose depositions on a tumour and the surrounding tissue for photons (left) and carbon (right). [21]

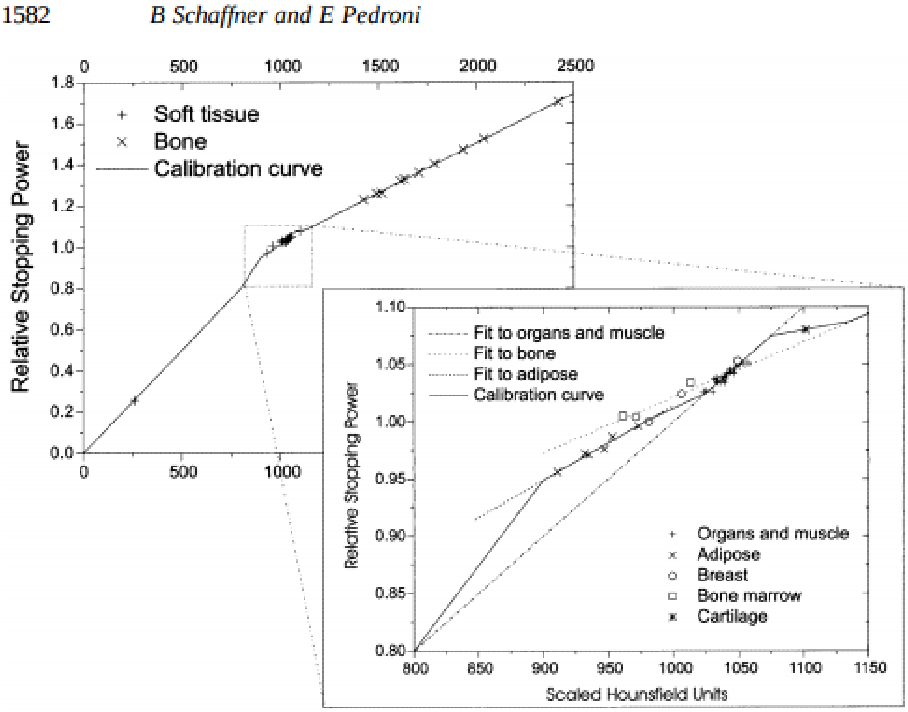

Figure 3.4.2: Calibration curves from HU to stopping power. [17]

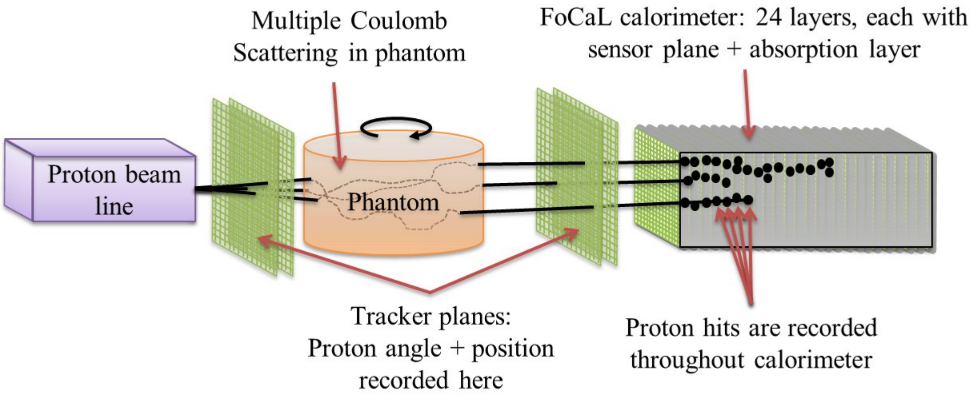

Figure 4.0.1: Schematic view of a pCT setup.

4 Proton Computed Tomography

As seen in the last chapter there are some intrinsic uncertainties connected to using X-ray CT to determine the stopping power for protons. The goal for proton CT is to measure the residual proton energy after having the beam pass through the target. It can then reconstruct the water equivalent path lenght in the target. The main difference between X-ray CT and proton CT is that regular CT is a statistical process where one count the number of photons one can collect. In proton CT one will expect to detect all of them. And the energy and vector of every single one needs to be collected.

A standard setup for proton CT is shown in figure 4.0.1. It consists of four external silicon pixel detector layers (two in front of, and two behind the target) and a calorimeter. The external detector layers are there to detect the trajectory of the protons before and after the target. This way the most likely path through the target can be determined. The protons then enter a sampling calorimeter that will determine the residual energy of the protons. About 100 protons are needed per 1 mm^3 voxel which corresponds to about 1 billion protons for a head size target. Ideally one would want to get a scan done in about 1 second so a detector capable of reading out data in GHz is needed for proton CT.

5 Detector characterisation with electron and hadron beams

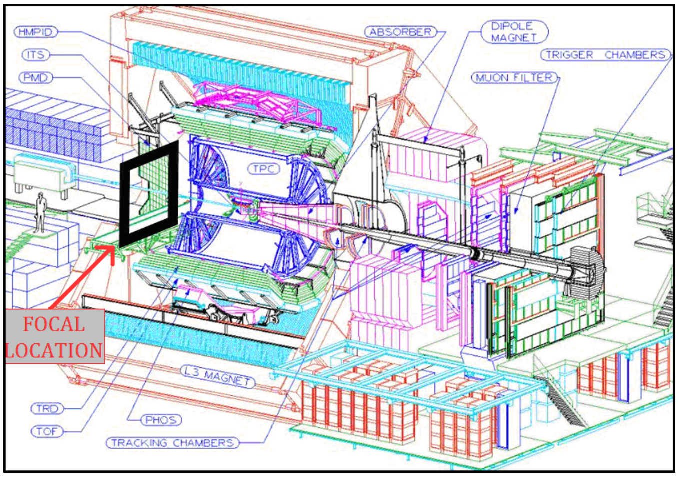

Figure 5.0.1: Basic schematic of the ALICE detector. The proposed position of FoCal is shown in black [3].

The FoCal (Forward Calorimeter) project is a proposed upgrade for ALICE (A Large Ion Collision Experiment) at CERN LHC. The forward positioning of the detector will allow for measurement of very high energy particles that stay close to the beam line. The main focus would be to measure prompt photons from interactions involving very low Bjorken-x and gluon saturation, but electrons/positrons and jets at these high energies may also be measured. One of the most important problems to solve at these energies is to be able to distinguish direct photons from decay photons (especially π^0 decay). Very high detector granularity is needed for this [6].

The current prototype has dimensions of approximately $4x4x10cm^3$ and consists of 24 layers of tungsten ($\approx$ 3.3 mm), and silicon and PCB ($\approx$ 1 mm). The remaining $\approx$ 2 cm comes from an extra thick layer of tungsten between layers 22 and 23. Each chip layer is made up of 4 MIMOSA-23 (Minimum Ionising Metal-Oxide Semiconductor Active pixel detector) chips at $\approx$ 2x2 cm^2 with 640x640 pixels each ($\approx$ 40 million pixels in total). The pixel size is 30x30 μm^2. The read out time for the current prototype is 1μs per pixel row in each chip totalling 640 μs per chip with a rolling shutter mechanic. All the chips are read out in parallell so the total time is still 640 μs. There is no zero-suppresion installed in the prototype so both read out time and amount of data (currently ≈ 8 GB/s) can be reduced [6].

5.1 PS and SPS experiments

Experiments have been carried out at the Proton Synchrotron (PS) and Super Proton Synchrotron (SPS) at CERN in September and November 2014 respectively to test the prototype's detection properties in a high-energy setting. At the PS the detector was put in a beam of electrons, muons and pions with momenta of 2–10 GeV. At the SPS the beam momentum varied from 30–250 GeV. Acquiring good statistical data during the experiments was a long process an outdated network card made the data transfer of one frame take about 2 minutes. This meant that data taking had to be done around the clock during the allowed beam times.

5.1.1 Data Acquisition

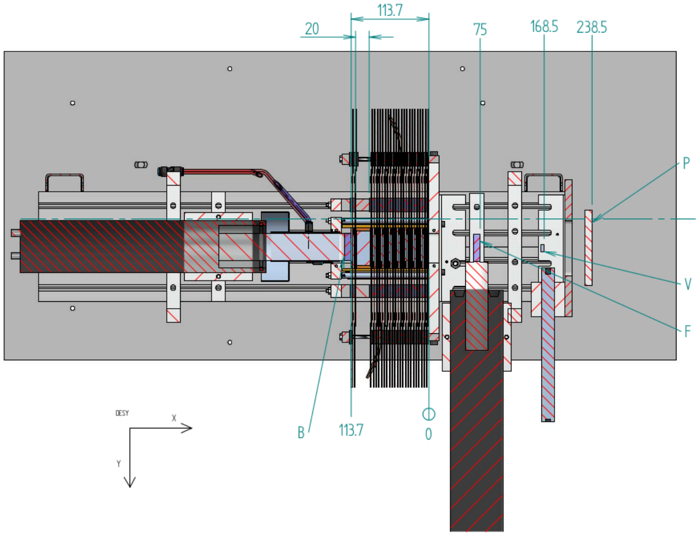

Figure 5.1.1: Schematic of the prototype setup showing the locations of the P, H, V, F, and B scintillators.

The prototype detector has two main modes for experiments; beam mode and pedestal mode. In beam mode the detector needs an external signal for when to read out data while the pedestal mode takes data continuously. Beam mode is suited for tests at accelerators like the PS and SPS since it will only receive short bursts of the beam, so called beam spills. A set of counting scintillators was used to trigger the data taking during these beam tests. The placements of these scintillators are shown in figure 5.1.1. The scintillators were called Present (P), Horizontal (H), Vertical (V), Front (F), and Back (B). The prototype was set to take data when we had a signal coincidence from these scintillators.

During the setup of the experimental equipment these scintillators had to be calibrated so that the output signals coincided in a desirable way. This was done by making sure that each signal went through an appropriate length of wire and delay boxes. The scintillator plateu also had to be found by adjusting in order to minimise fluctuation in signal counting. Čerenkov detectors were also utilised during the PS test to distinguish between pions/muons and electrons.

5.1.2 Pedestal Runs

Between every data taking run a pedestal run was carried out. A pedestal run is a data run where data is taken without the presence of a beam. This helps identify which pixels have the most tendency to produce a fake hit. While processing the real data, the most noisy pixels were removed according to the threshold settings. The standard threshold setting was 10^{-5}, which meant that on average only 1 in 100 000 pixels was considered noisy after the removal of the most noisy pixels. This setting corresponds to about 16 noisy pixels per layer (1280x1280 pixels) after processing. Even with a high threshold setting the sheer number of pixels still allows for reasonable statistics. The large number of pixels is key since there is a lot of things that can go wrong in such a complicated system. Whole lines of pixels may be noisy and some channels or even chips may be dead. An overview of dead channels and chips is shown in figure 5.1.2.

5.1.3 Results

Some of the results from the PS test are shown in figures 5.1.3 and 5.1.4. The plots show the number of pixels fired in relation to event occurence. The black curve in both figures is from pedestal runs, so there is no beam present. In figure 5.1.3 the tall red peak is from particle tracks of muons and pions, while the smaller and wider peak is caused by electromagnetic showers from electrons. Figure 5.1.4 shows the same data, but trigger signals from the čerenkov detectors have been used to filter out the muons and pions.

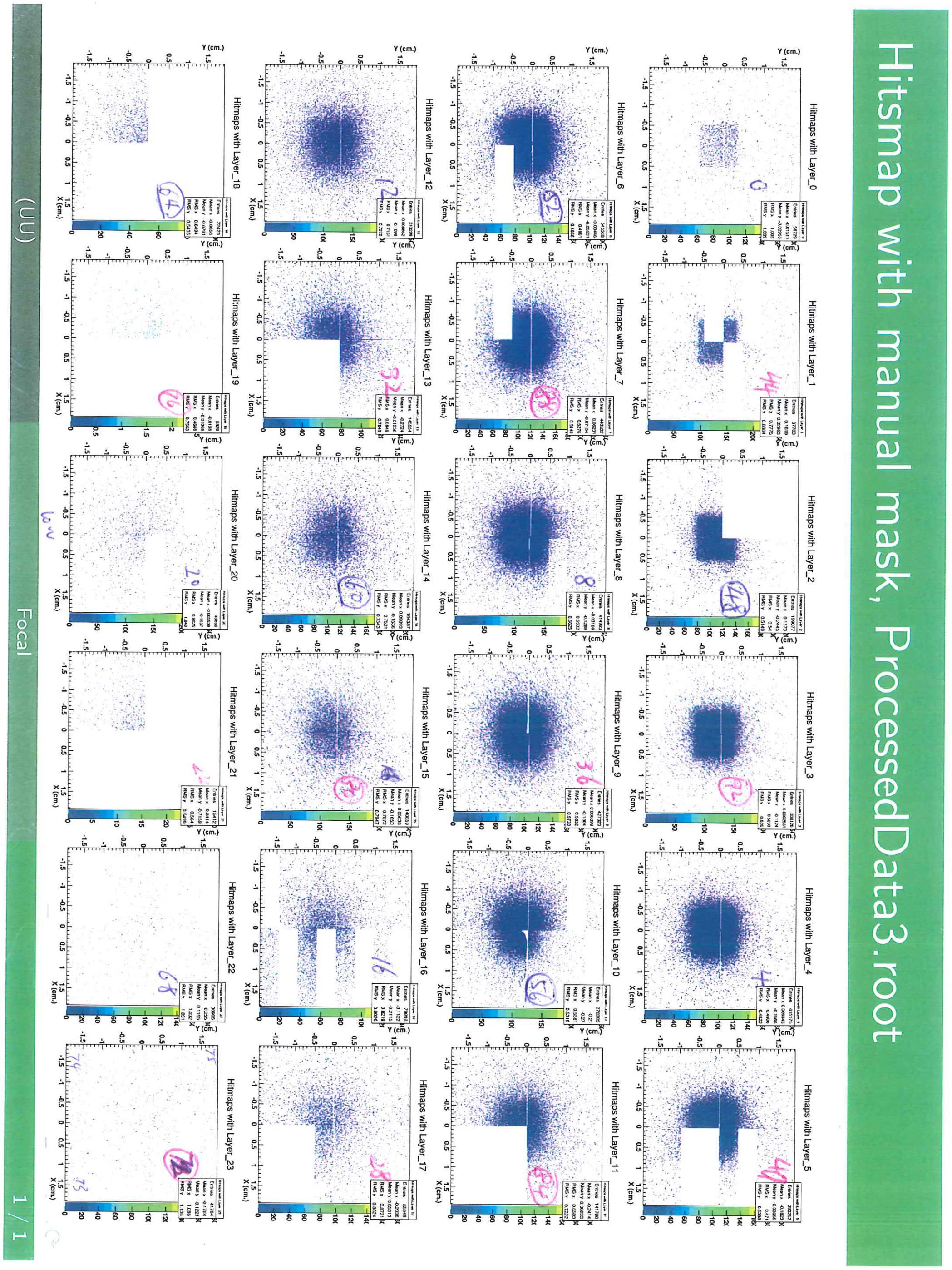

Hitsmap with manual mask, ProcessedData3.root

(UU) Focal 1 / 1

Figure 5.1.2: Hits map for the whole detector with an EM shower present. It is possible to see which layers have dead channels and chips.

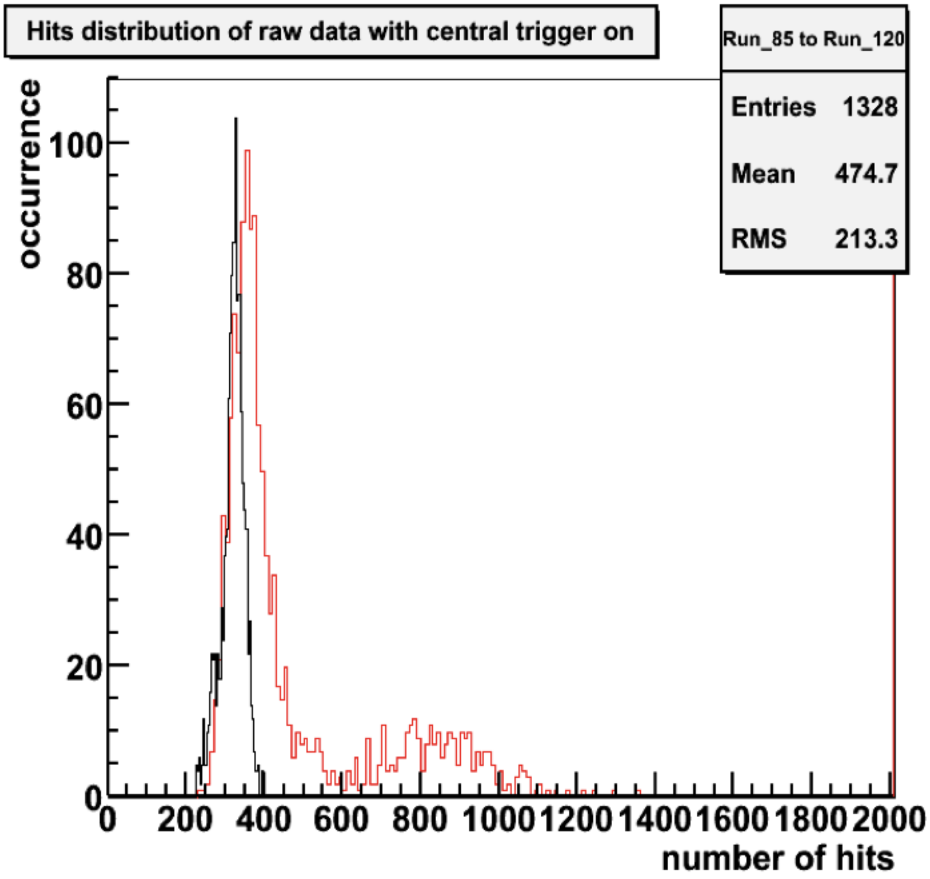

Figure 5.1.3: Hits distribution from 2 GeV momentum runs at the PS. The black line is from a pedestal run. The big red peak is from particle tracks and the smaller cluster to the right is from EM showers. Plot was provided by Elena Rocco.

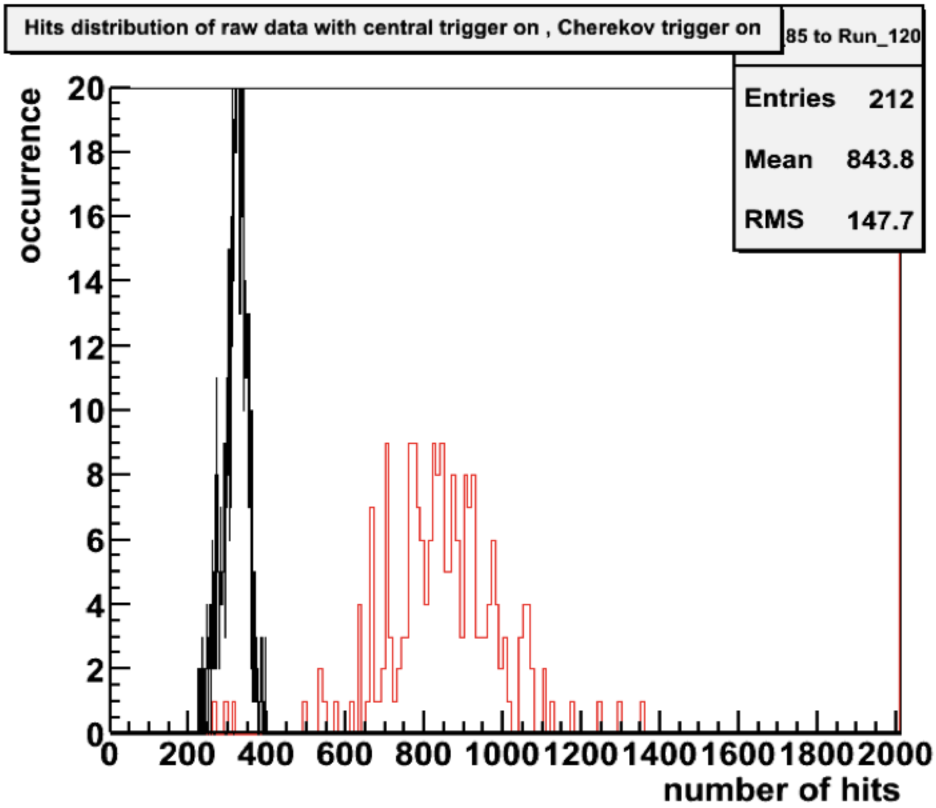

Figure 5.1.4: Filtered hits distribution from the same runs as figure 5.1.3. The black line is from a pedestal run and the smaller cluster to the right is from EM showers. Provided by Elena Rocco.

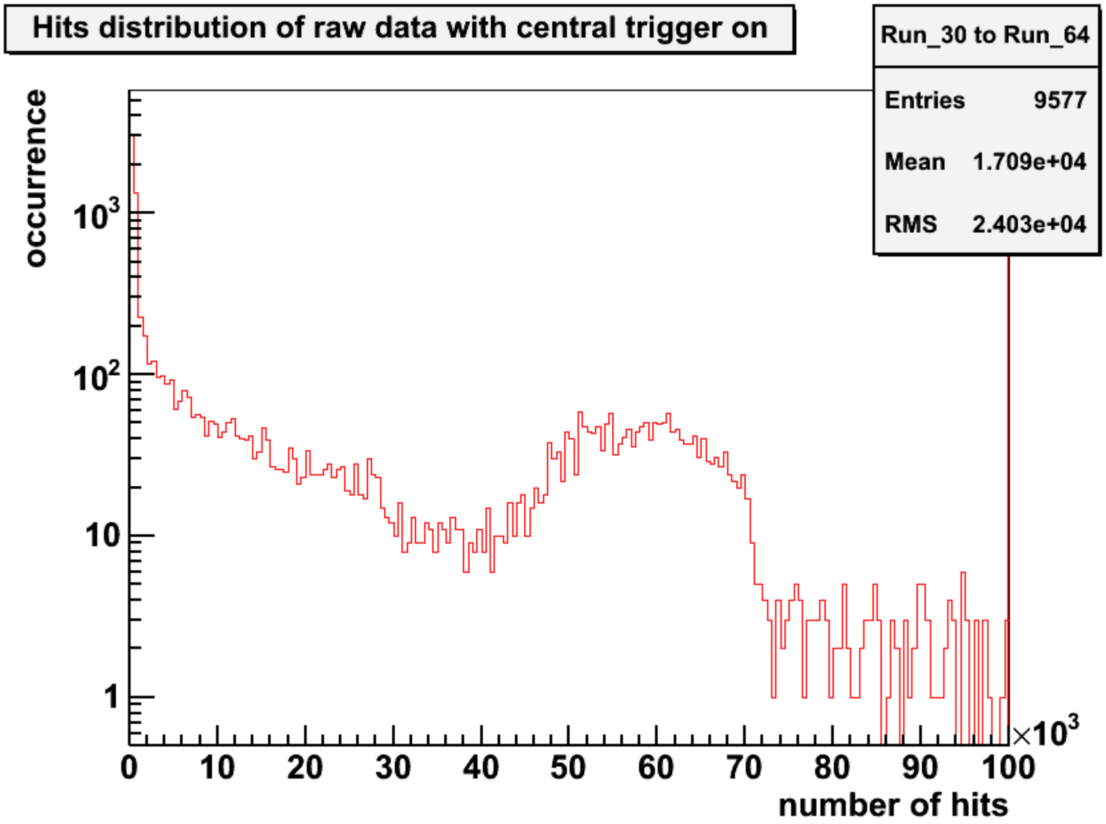

Figure 5.1.5: Hits distribution from 250 GeV momentum beam spills. The cluster to the right is from developed EM and hadronic showers. The peak to the left is particle tracks. Everything in between is from partially developed showers. Plot provided by Elena Rocco.

5.2 Monte Carlo and FLUKA

Simulations were done based on the FLUKA input file from [1] with slight modifications to the geometry. An absorber layer was added in front of the detector to make it more like the real prototype. Simulations at the same nominal energies as the experiment in the next chapter were then carried out in order to determine the mean energy loss in each layer.

6 KVI Results and Discussion

The KVI-CART (KVI - Center for Advanced Radiation Technology) is a research center for subatomic and astroparticle physics located on the campus of the University of Groeningen, the Netherlands. In one of their facilities they have a superconducting cyclotron capable of provding particle beams with protons and ions with charge-mass ratios of 0.1–1.0. They can provide proton radiation with energies up to 190 MeV and heavier ions, like Xenon-124 can be at 30 MeV/u.

The purpose of the beam test at KVI with the FoCal prototype was to investigate if the pixel based digital sampling calorimeter is suitable for use in proton computed tomography. Some parameters we will look at are Bragg Peak position, proton scattering and tracking, and charge diffusion in the chip. A suitable detector for pCT needs to be able to distinguish between individual particles and acquire information about their individual paths and energy deposition. Tests at a range of energies were carried out, but limited beam time meant that we have low statistics. The beam time was further reduced by problems with the accelerator.

The plots presented in this section are mostly based on C++/root scripts by PhD student Helge Pettersen who is also working in this field.

6.1 Experimental setup

In contrast to earlier beam tests where the beam was sent in spills, the KVI beam was continuous. This meant that the detector could be kept in "Pedestal mode" and take data continuously instead of relying on the trigger system to tell it when to take data. Events were recorded with the F and HV scintillators though. They were used to give us a rough feeling of the particle rate and let us filter data based on coincidence between the scintillators. The beam intensity was regulated by the beam control center on request to keep the particle flux approximately constant as we changed between different energies.

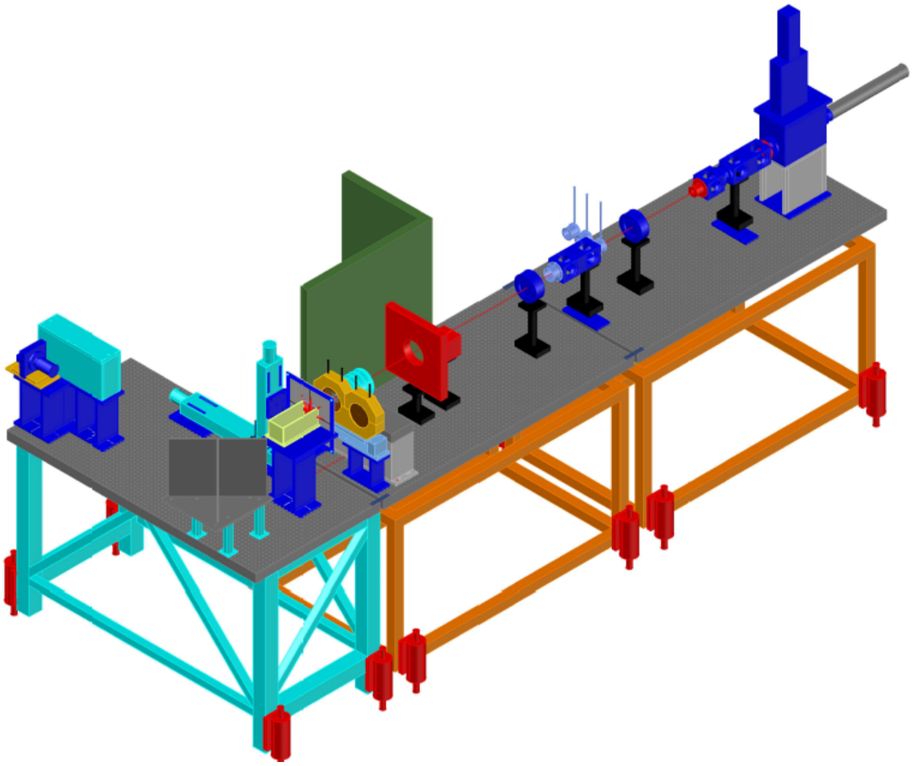

Figure 6.1.1: 3D schematic of the beam line at KVI where we can see the various beam line components [22].

Before the real beam testing started a simple model was used to determine some energies that would have the Bragg peak very close to a sampling layer. We assumed the base energy of the cyclotron would be 190 MeV, but that was a naive assumption. The output energy of the accelerator is 190 MeV with energy resolution typically better than 0.25%. But with about 3 meters of air and scatter foils in between the beam line and the target the energy will be lower. Typically 5-10 MeV is lost before the beam hits the target. The naive energies we chose were 190 MeV, 170 MeV and 122 MeV. The beam energy was adjusted with aluminium beam degraders that were inserted to the beam line by a remote controlled hydraulic system. These were of varying thicknesses, allowing for a wide range of energies.

The beam was broadened and flattened by a scattering foil system and then collimated to a diameter of 70 mm at the target location. The radiation field is homogeneous to about 3% at this size.

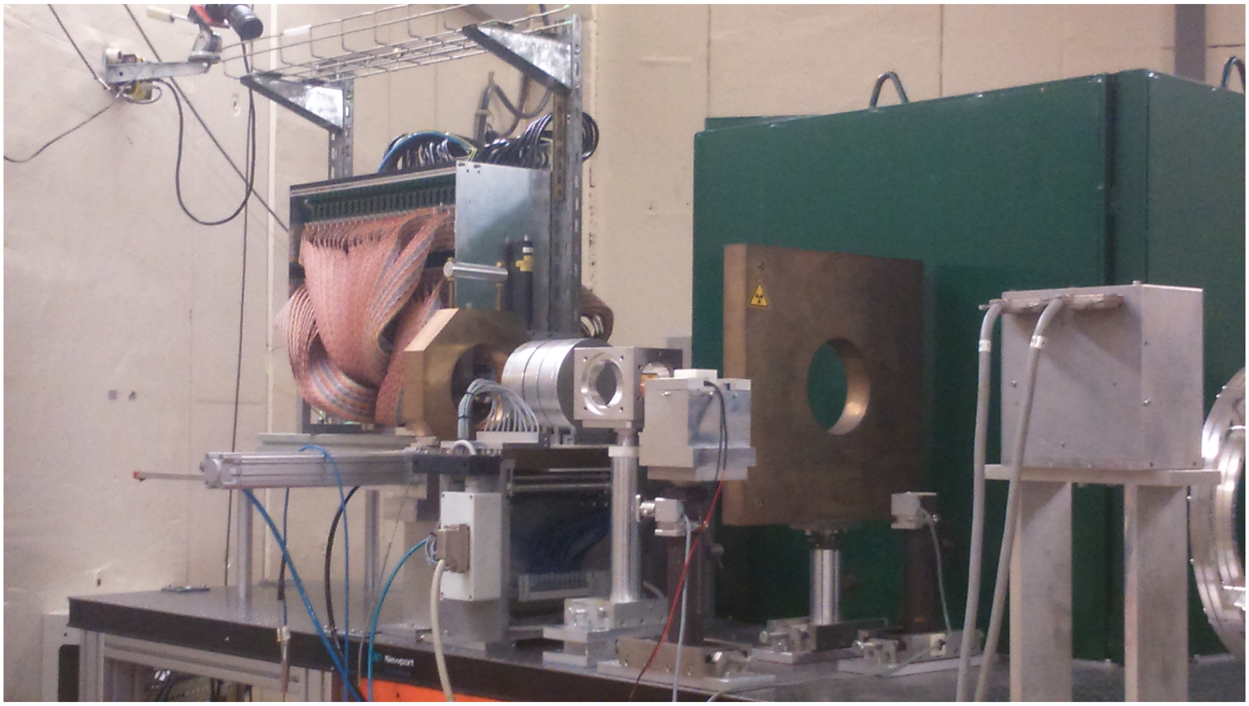

Figure 6.1.2: The FoCal equipment on the breadboard in the KVI beam room. We can also see the copper collimators. Between the collimators we can see the aluminium disks we used to adjust beam energy.

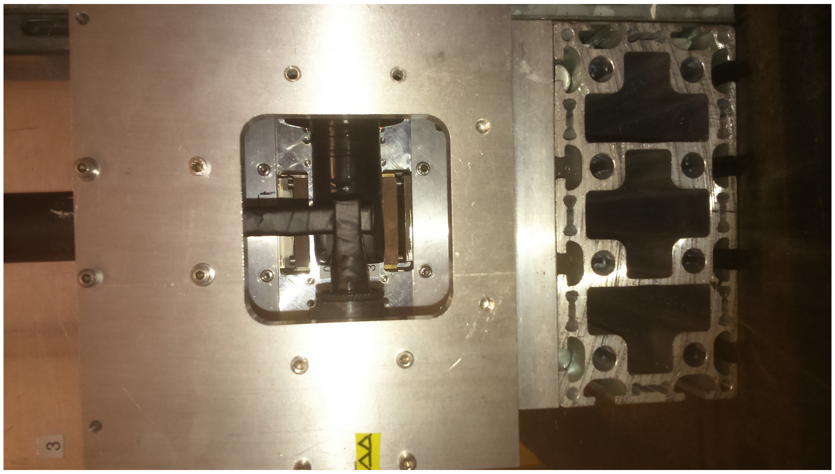

Figure 6.1.3: The FoCal detector seen from the front. We can see the H and V scintillators at the front and the F scintillator behind them.

6.2 Charge Diffusion in MAPS

It is useful to understand how electron-hole pairs spread out inside the epitaxial layers of the MAPS chips when looking at detector response. They will, in principle, diffuse thermally in any direction from a particle track as shown in figure 2.4.3. The free electrons move around randomly, but are kept from exiting the epitaxial layer (which is lightly P doped) because of the potential difference between the it and the highly P doped substrate. Eventually they will either recombine back to the valence band, or they will be collected in the N-well diode.

The thermal diffusion of the free electrons means that an isotropical charge distribution is to be expected. Which also means that observed clusters should be symmetric around the seed pixel for incident angles close to 0°. There is a clear elongation of the pixel cluster at larger angles, as shown in figure 6.2.1. Figure 6.2.2 shows how incident angle is related to the number of pixels containing 90% of the electrons, and the expected number of electrons freed. It makes sense that those curves increase with the incident angle as they depend on the particle path length through the active part of the detector [15]. Figure 6.2 shows cluster shapes at different cluster sizes from the KVI beam test. The clusters tend to be symmetrical, but there is some deviation. MIMOSA-5 and MIMOSA-18 have pixel sizes of 17 μm and 10 μm respectively, and the cluster elongation is heavily dependent on incident angle θ for θ larger than 55 deg and 45 deg respectively. Cluster elongation can not be reliably determined below these values [15]. Since MIMOSA-23 chips have 30 μm pitch it is expected for them to be even less sensitive to the incident particle angle. The asymmetry in some of the clusters in figure 6.2 may be caused partially by the incident angle, even though it should be small. Chip noise may also be a contribution.

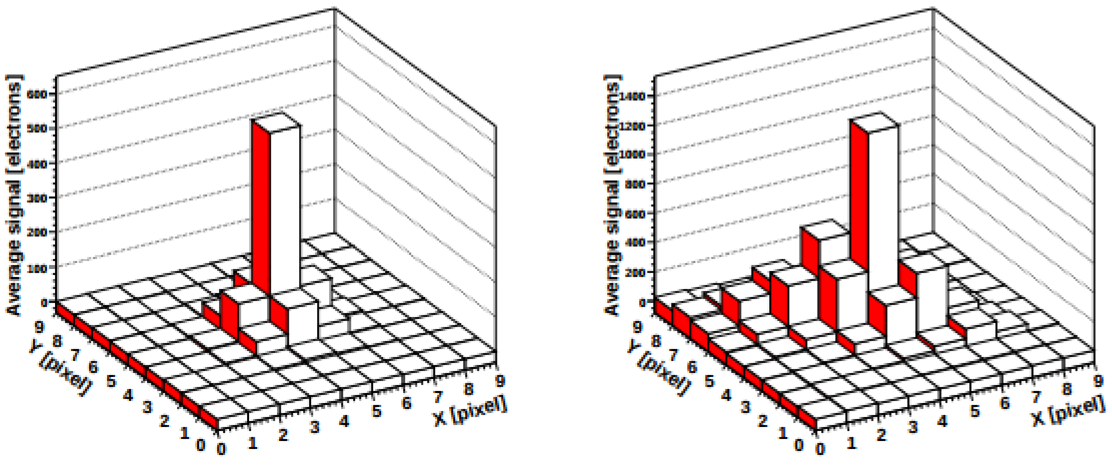

(a)

(b)

Figure 6.2.1: Charge distribution at different incident angles (4.3 degrees in a and 78.1 degrees in b) for the MIMOSA-5 chip (17 μm pitch). The values shown are the average values with a 6 GeV electron beam [15].

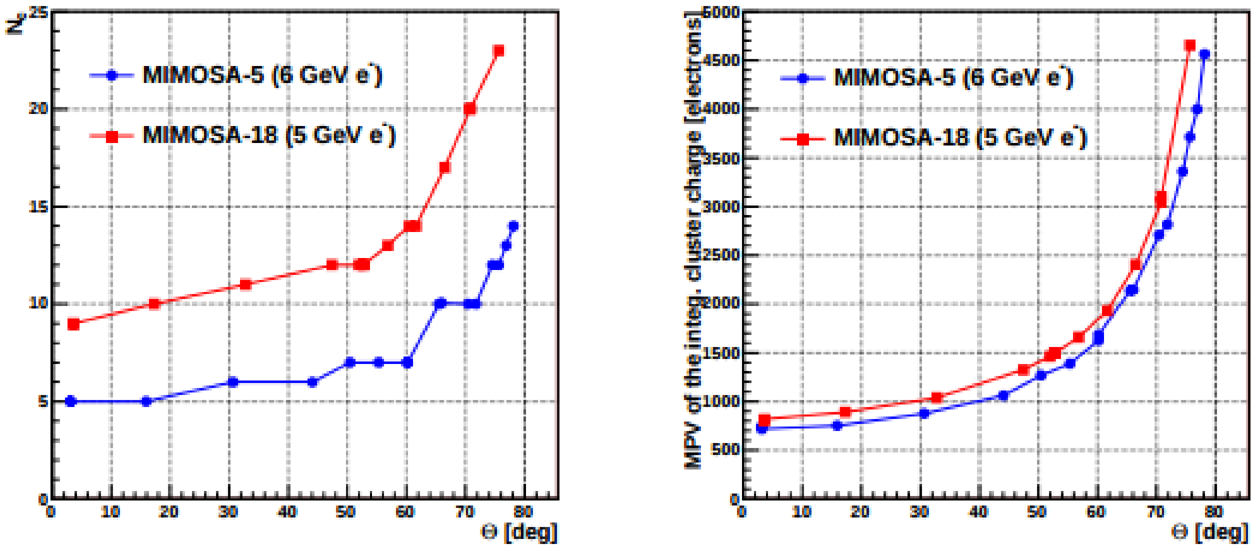

(a)

(b)

Figure 6.2.2: a) The number of pixels containing 90% of the freed electrons at different incident angles. b) Most Probable Value of liberated electrons at different angles. MIMOSA-18 chips have 10μm pitch. [15]

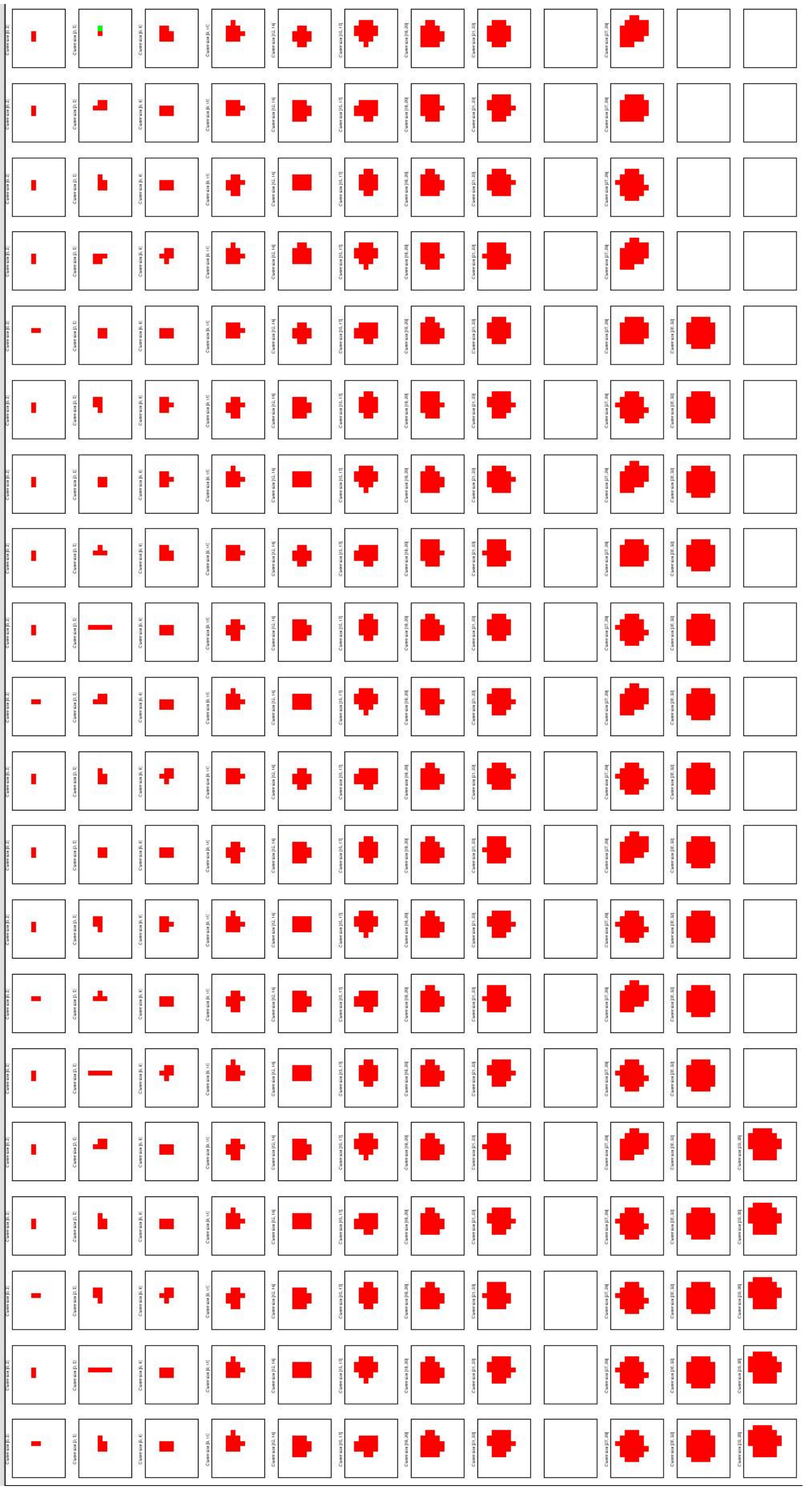
Cluster size [0, 2]
Cluster size [3, 5]
Cluster size [6, 8]
Cluster size [9, 11]
Cluster size [12, 14]
Cluster size [15, 17]
Cluster size [18, 20]
Cluster size [21, 23]
Cluster size [27, 29]
Cluster size [30, 32]
Cluster size [33, 35]

6.3 Particle Tracks

When tracking a particle passing through the detector we have to look for the particle's "footprint" – a pixel cluster. Tracks are then generated by looking at cluster positions in subsequent layers and matching them to a track. By assuming that the electrons spread out uniformly it is possible to find the weighted center of a cluster which is then assumed to be a point on the proton path. Since the protons mostly lose energy by ionisation, the path length should be relatively well defined with relatively low deviation for most of the protons. This is caused by the random nature of the ionisation loss. Some proton tracks will be considerably shorter than the rest due to rare, high energy transfer interactions like nuclear interactions. Additional variations in the measurable path length come from multiple Coulomb scattering. In order to measure the track lenght one have to calculate the distances between the points where particles have been detected. In this thesis this is done simply by taking the straight line between points, but there exists algorithms that allow us to calculate the most likely paths.

We can mostly see this expected behaviour in figure 6.3.1, 6.3.2, and 6.3.2. Due to the thinness of the sensitive layers of the detector, compared to the thick absorbers, the latter part of the distribution is lost and the protons are counted in the last bin.

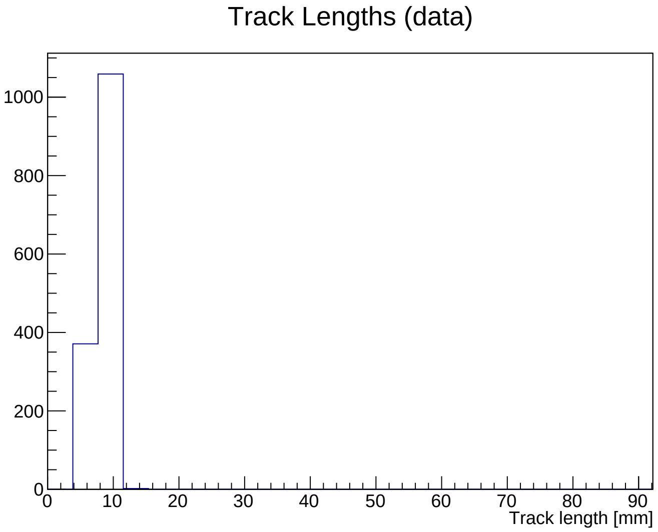

Figure 6.3.1: Path lenght distribution for 122 MeV protons.

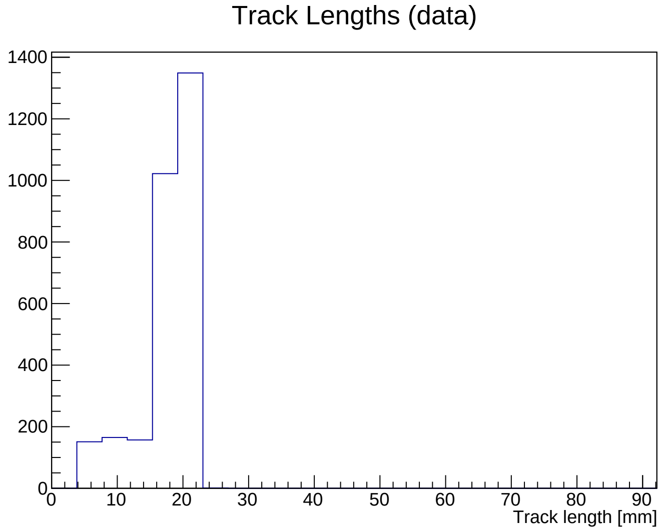

Figure 6.3.2: Path lenght distribution for 170 MeV protons.

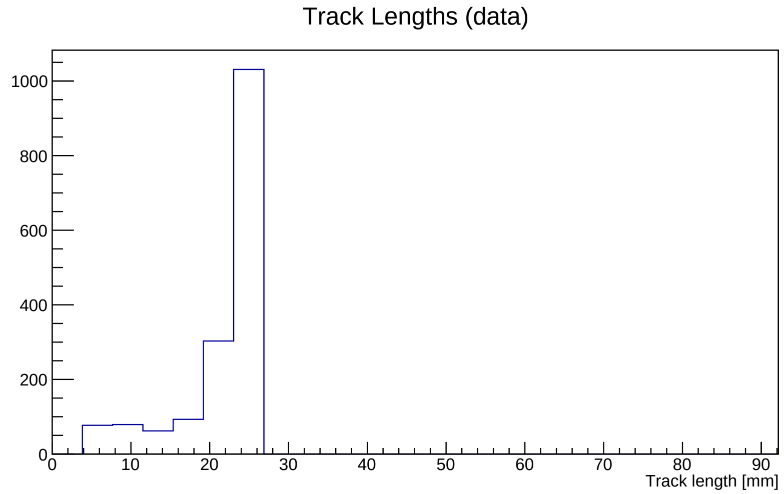

Figure 6.3.3: Path lenght distribution for 190 MeV protons.

Protons going through matter will be scattered from their trajectories by interactions with atomic nuclei. As mentioned in chapter one, the scattering angle should have an Gaussian distribution with the average angle given by equation 10 as

$$\theta_0 = \frac{13.6MeV}{\beta cp} z \sqrt{\frac{x}{X_0}} \left[1 + 0.038 ln(x/X_0)\right]. \tag{28}$$

We can see that this quantity should be lower for higher energies and it should increase with the penetration depth. The total scattering angles are shown in figures 6.3.4, 6.3.5, and 6.3.6 below. These are found by simply calculating the angle between the first and last point where a specific proton is detected. We can see that the average values for the total scattering angle stays about the same. It is also interesting to see how the scattering angle changes from layer to layer. Angle distributions for scattering between the first and the indicated layer are shown in figure 6.3.7, 6.3.8, and 6.3.9 for 122 MeV, 170 MeV and 190 MeV respectively. There is a clear tendency for the scattering angles to increase as the protons deposit energy in the detector which we would expect from how equation 28 depends on energy.

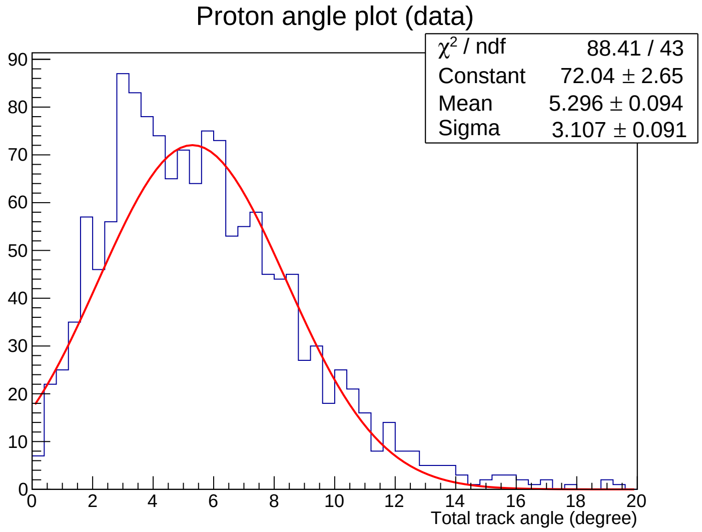

Figure 6.3.4: Distribution of the total scattering angle for 122 MeV protons

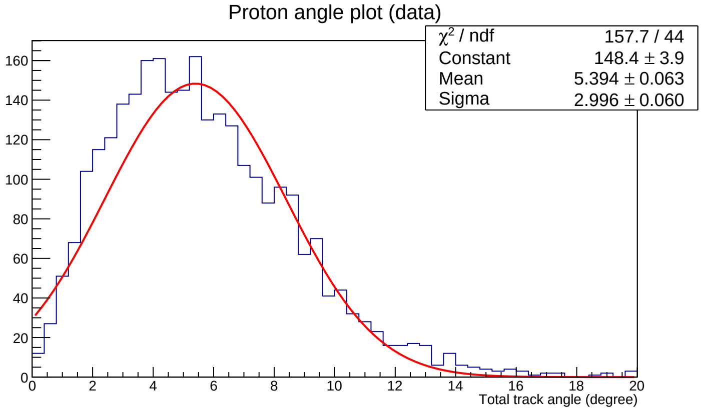

Figure 6.3.5: Distribution of the total scattering angle for 170 MeV protons

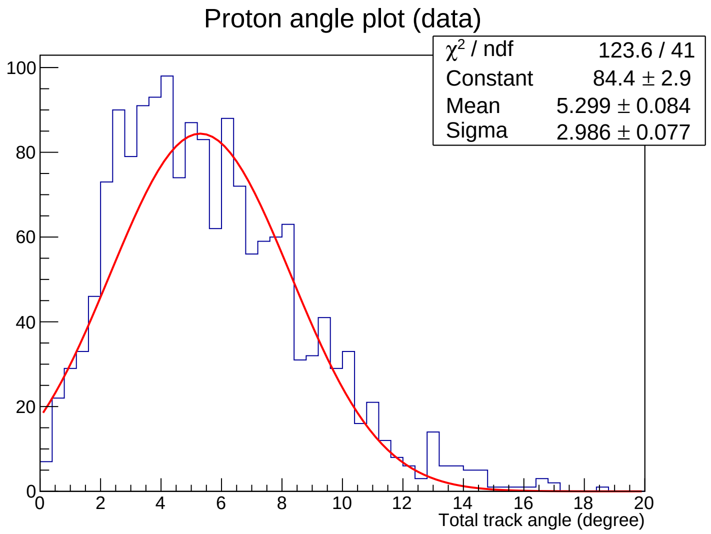

Figure 6.3.6: Distribution of the total scattering angle for 190 MeV protons

By using the mean from the total scattering angle plots together with the nominal proton energy and measured track lengths (we will come back to those later) it is possible to calculate the expected scattering angle from equation 28. The radiation length of the detector has been calculated to be 4.0 mm [1], [3]. The results of these calculations are shown in table 2. And to show the extent of the particle scattering, the ratios between total path lenght and the straight line between end points are shown in figure 6.3.10.

Energy [MeV]	Track lenght [mm]	Measured angle [degrees]	Estimated Angle [degrees]
190	24.68 ± 0.06	5.30 ± 0.08	5.95
170	20.68 ± 0.02	5.40 ± 0.06	6.0
122	9.49 ± 0.08	5.30 ± 0.09	5.39

Table 2: The table shows the measured scattering angles together with estimated angles and relevant variables.

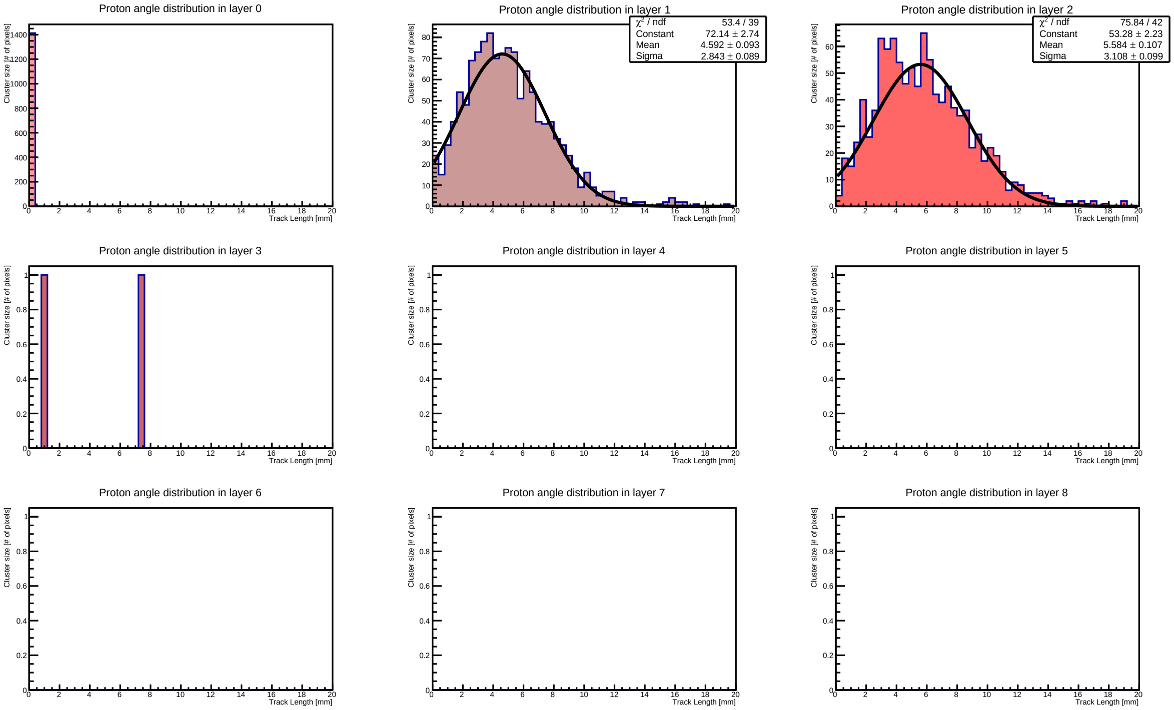

Figure 6.3.7: Scattering angle between layers for 122 MeV protons.

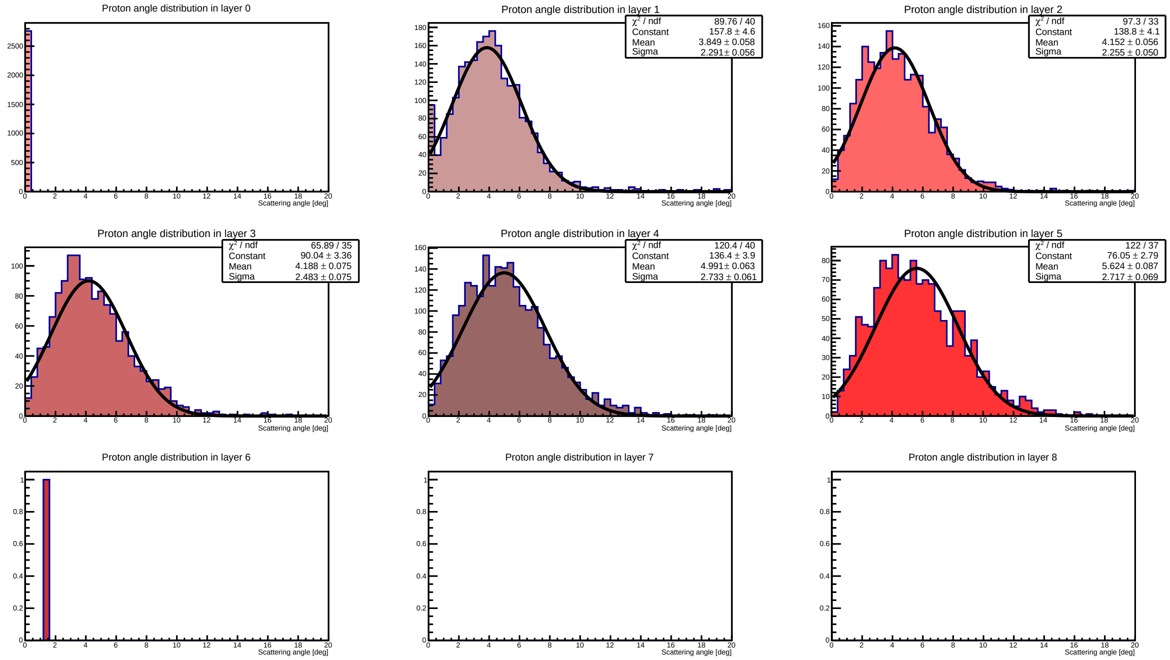

Figure 6.3.8: Scattering angle between layers for 170 MeV protons.

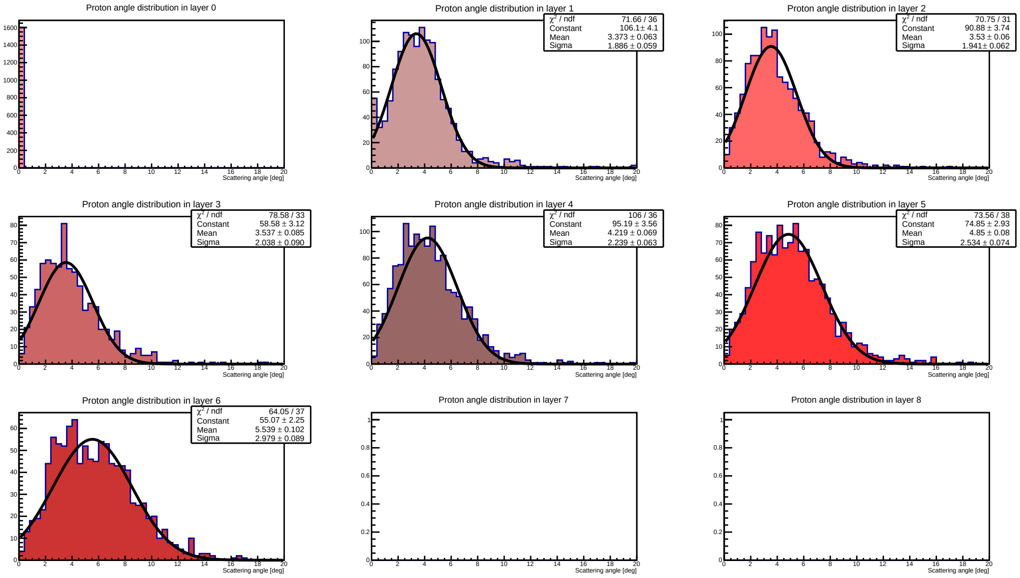

Figure 6.3.9: Scattering angle between layers for 190 MeV protons.

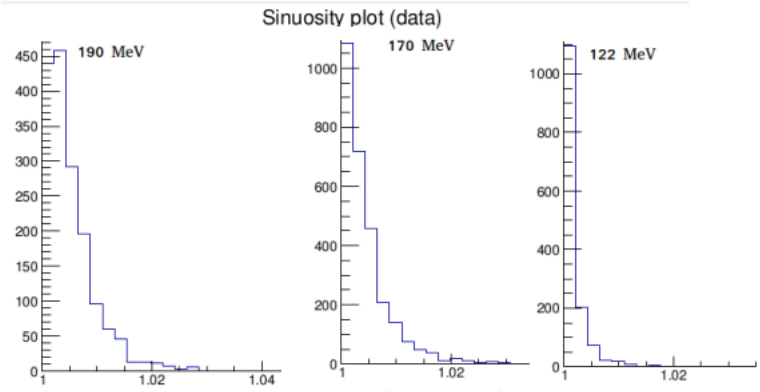

Figure 6.3.10: The curviness (sinuosity) parameter for the path lengths of the three different energies. We can see that the scattering does not matter much in terms of path length.

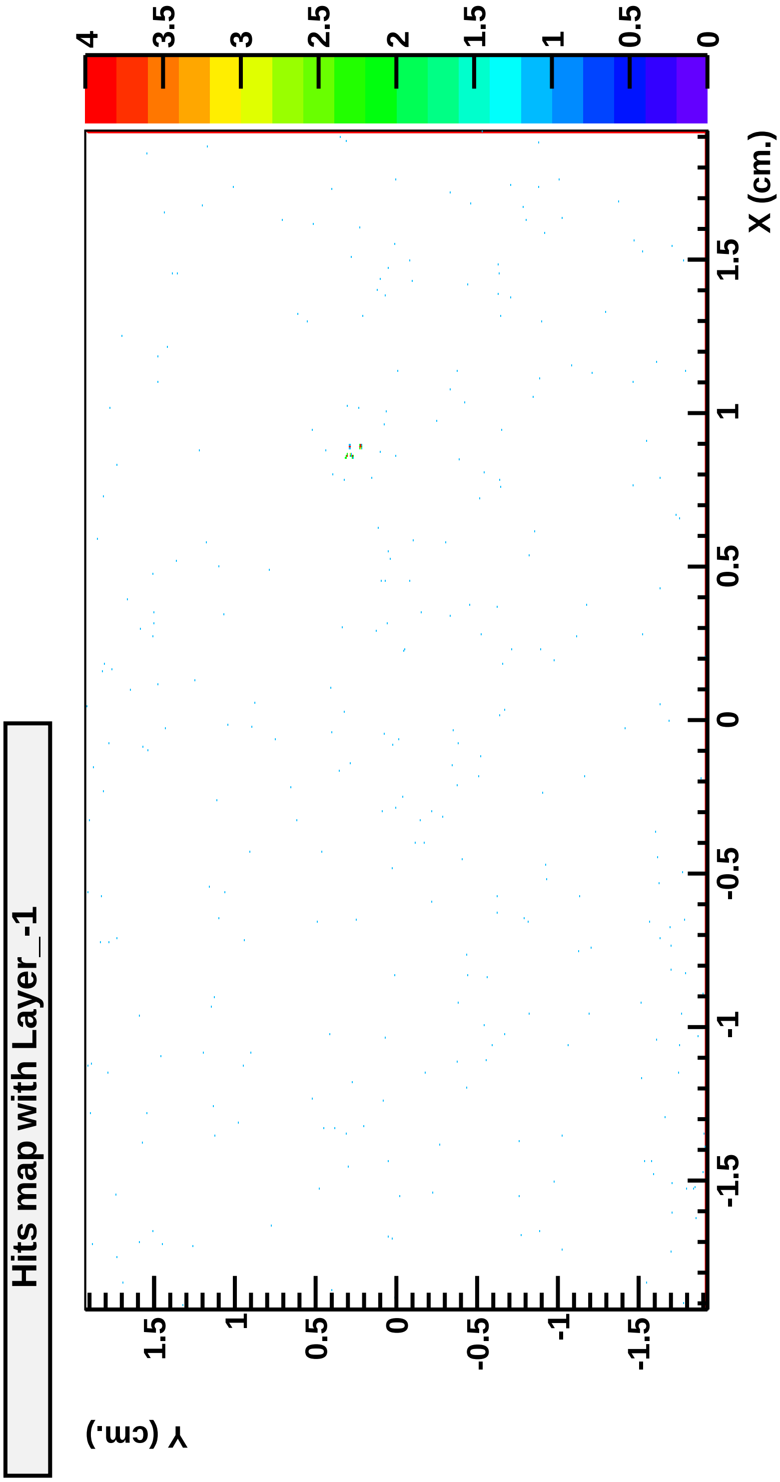

Figure 6.3.11: Super position of hits from all layers for a single proton event from KVI. We can see that the proton stays in the same area at about 1 cm x and 0.5 cm y coordinates.

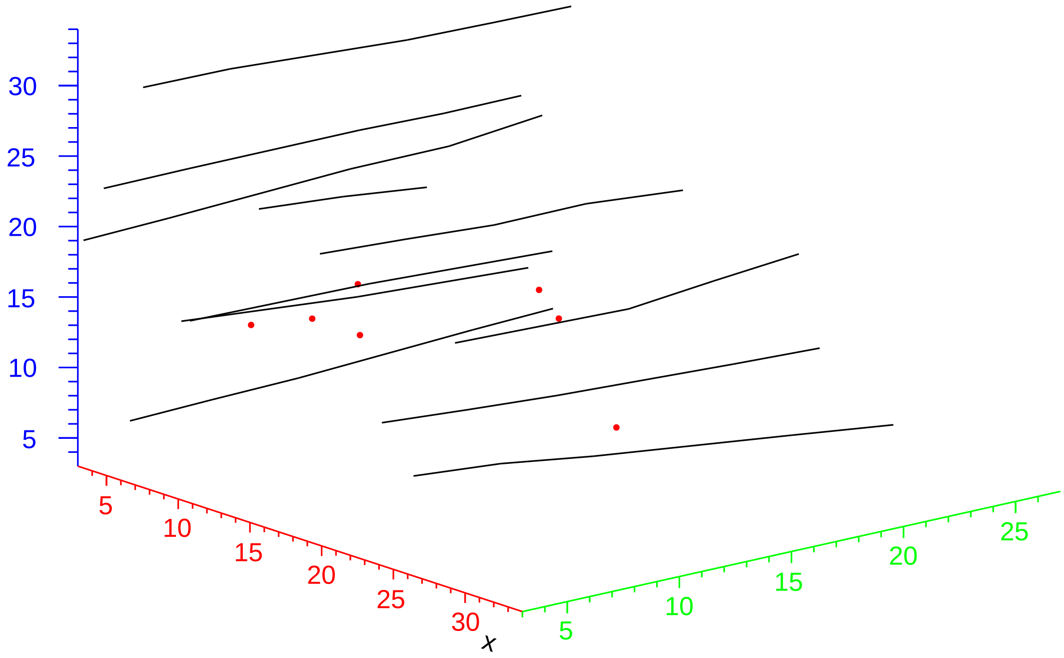

Figure 6.3.12: Handful of tracks from a 190 MeV run plotted in 3D.

6.4 Pixel Clusters and the Bragg Peak

It is possible to make a couple of predictions about the behaviour of cluster sizes for changes in incident energy and detector depth from equation 5 and figure 1.2.1, assuming that we are in the non-relativistic domain. In the early layers of the detector one will expect the average cluster size to decrease as incident energy increases as the material stopping power will increase until the particle becomes relativistic. And as the particle traverses the detector energy deposition should increase and cluster size should increase with it. It was stated earlier that the energy deposition in the active layers of a sampling calorimeter follows a Landau distribution. It is then reasonable to assume that we get a Landau distribution for the cluster sizes in the various layers of the detector. We can see in figures 6.4.1, 6.4.2, and 6.4.3 that a Landau curve fit suits most of the cluster size distributions reasonably well. In the later layers it becomes apparent that energy straggling and differences in path length due to multiple scattering takes effect as the cluster size spread increases.

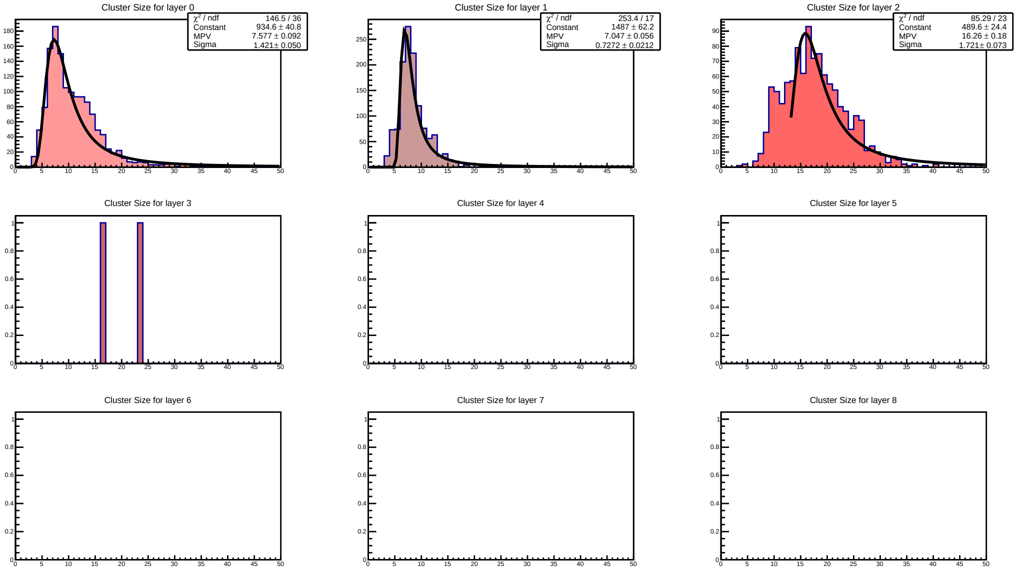

Figure 6.4.1: Cluster size distribution for the different layers for 122 MeV protons.

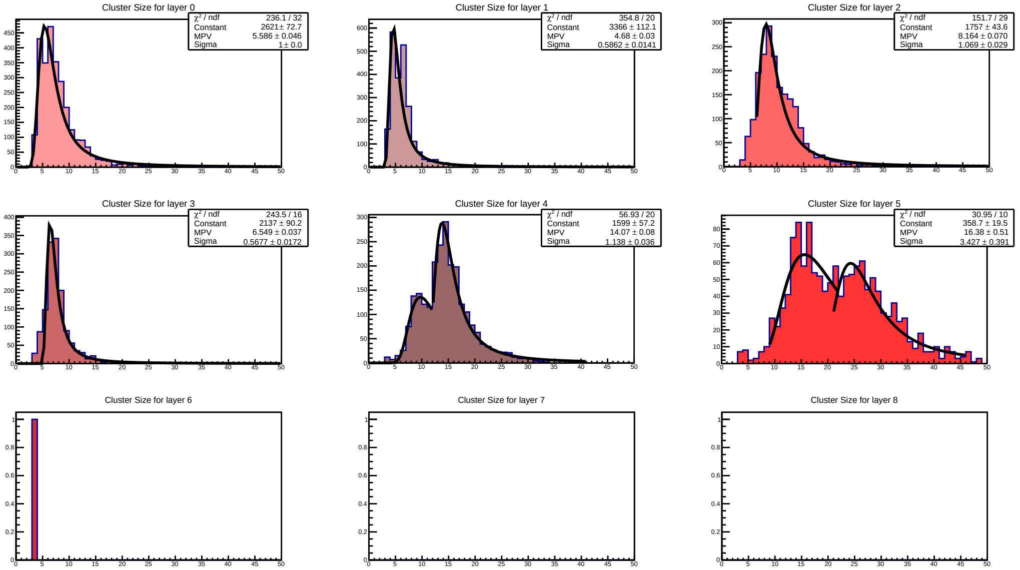

Figure 6.4.2: Cluster size distribution for the different layers for 170 MeV protons

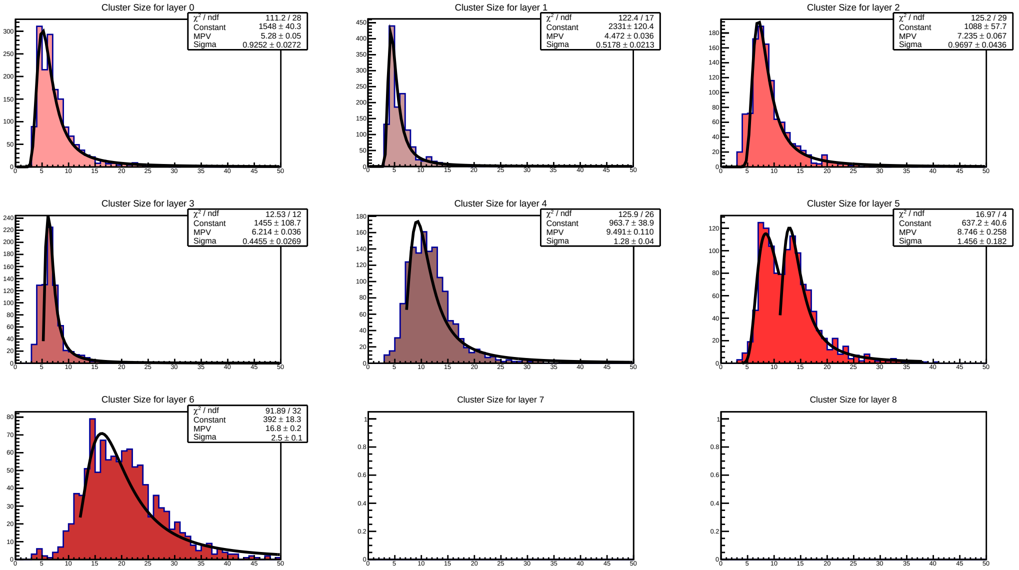

Figure 6.4.3: Cluster size distribution for the different layers for 190 MeV protons

For both 190 MeV and 170 MeV we get a clear double peak in the second last layer. In the case of 170 MeV we also get a less clear cut double peak in the last layer while the increased cluster size spread in the last layer for 190 MeV can be just plain straggling. To the first order it seems like the double peaks are super imposed Landau distributions, indicating two, slightly different proton energies. .

One possible reason for this behaviour is that we get a snowball effect in energy loss. If a particle undergoes slightly more than average energy deposition at one point the difference in path lenght between it and the average particle will increase further in. We know that charged particles deposit more energy as they slow down and that they are more susceptible to Coulomb scattering with lower momentum. This leads to a higher energy loss per unit length and a longer path between the sampling layers. By itself one would expect this energy loss factor to only produce a wide straggling range. Combined with a very large ratio between absorber volume and sampling volume, in addition to the large Z of tungsten compared to silicon, it could possibly produce this behaviour.

Additionally, the H and V scintillators does not cover the whole detector, so there might be differences in proton energies entering the detector. The scintillators have areas of about 30 mm x 10 mm each and overlap 10 mm x 10 mm [2]. They are however plastic scintillators [7] so the density is almost the same as water and their contribution is probably not too big. It might also be caused by something in the beam line itself. As mentioned earlier, the proton beam is at 190 MeV as it exits the accelerator, but loses on the way to the target amount to 5-10 MeV. This depends on how the beam is shaped and the profile flattened. Neutron production from beam line equipment or detector material could also be a contributing factor, but the expected neutron rates are too low to have this effect (order of 1 neutron per 1000 protons) [23].

Each layer of the detector is made from 4 MIMOSA chips with 4 channels each. These are subject to failure and noisy pixel rows etc. We can clearly see dead channels and chips in the different layers in figure 5.1.2. We also have differences in response for the different layers, as illustrated in figure 6.4.4 and figure 6.4.5. We can see that these relative differences stay approximately the same for both 170 MeV and 190 MeV, but ideally there should be close to no difference in response between the chips as the radiation field is

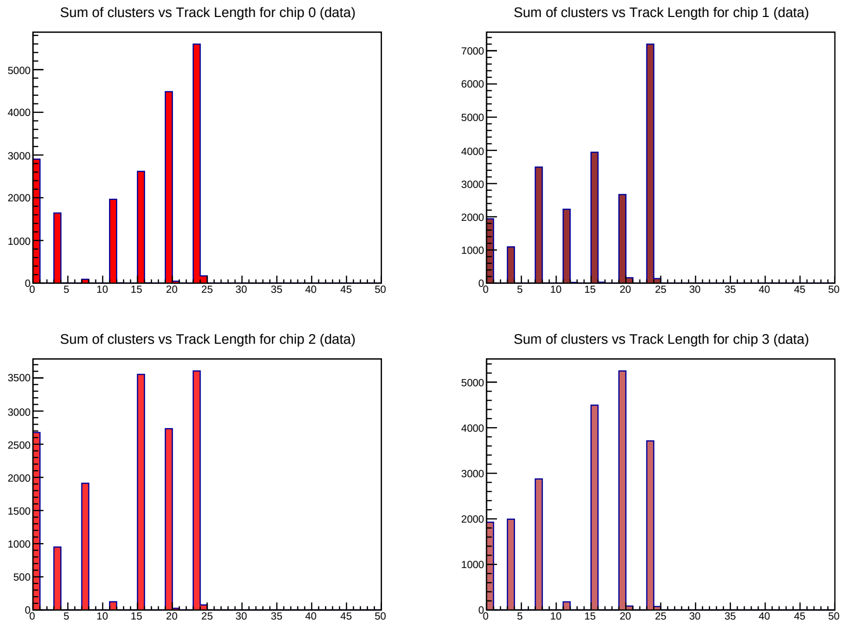
Sum of clusters vs Track Length for chip 0 (data)

Sum of clusters vs Track Length for chip 1 (data)

Sum of clusters vs Track Length for chip 2 (data)

Sum of clusters vs Track Length for chip 3 (data)

Figure 6.4.4: Detector response for 190 MeV protons split between the 4 chips in each layer. Response should be uniform across the chips for the same layers.

very homogeneous. We know that the chips are calibrated slightly differently in order to counteract things like gradient noise [1]. So it is plausible that different sensitivites can cause some of the double peak structures we have observed as a particle with the same energy will cause a different response in different chips.

By using the average values from the cluser size distribution plots together with average energy deposition in each layer from Monte Carlo simulations to make a plot relating these two quantities. 40 000 primary particles were used for each energy. The energy deposited in the simulations should be on the low side as I have ignored the beam energy loss from the beam scatter foil and about 3 m of air. The relationship between cluster size and deposited energy is shown in figure 6.4.6. A best-fit curve is found using the built-in fitting feature of gnuplot. The Best Fit curve is parameterised as

$$N(dE) = a \cdot dE^b = 0.025 \cdot dE^{1.681} \tag{29}$$

Standard errors for the fitting parameters a and b are given as ±0.015 and ± 0.16 respectively.

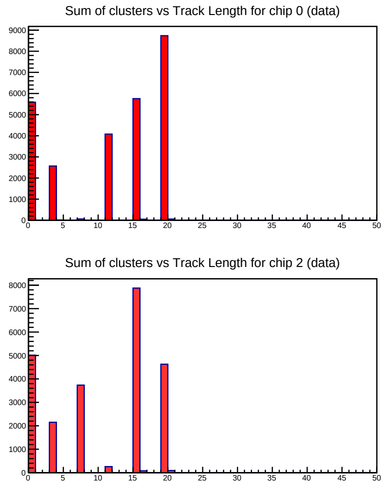

Figure 6.4.5: Detector response for 170 MeV protons split between the 4 chips in each layer.

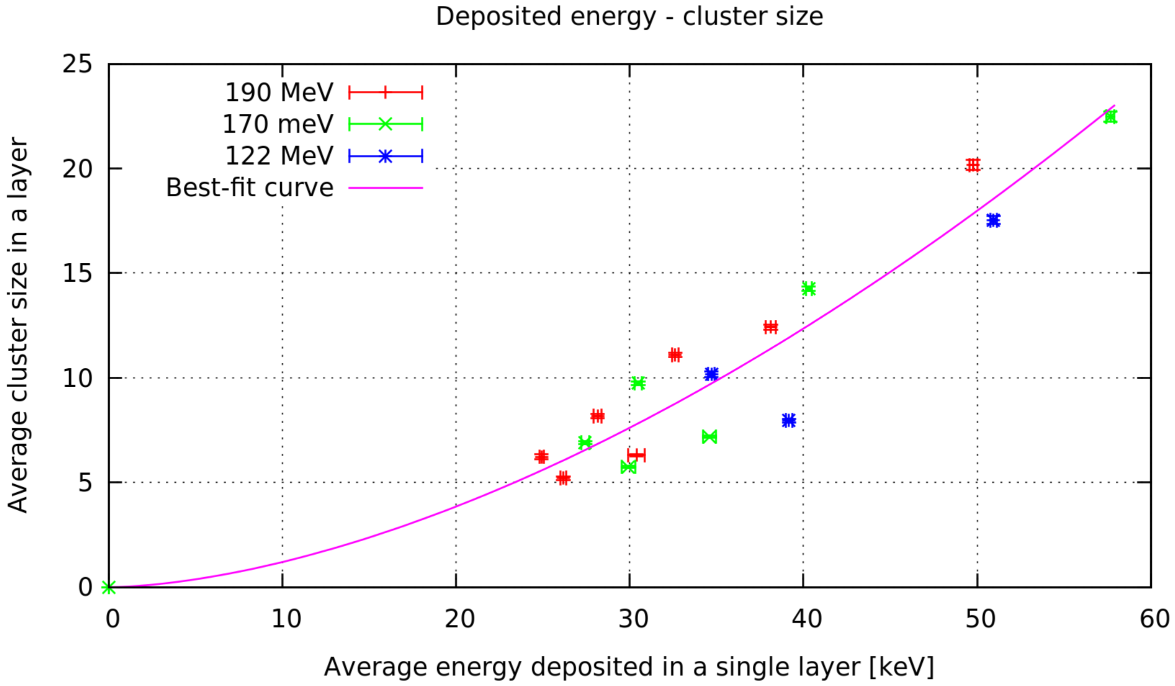

Figure 6.4.6: Relationship between estimated energy deposition in each active layer (based on MC) and average number of pixels fired in each layer.

With information about the length of a particle's track, how it varies as scattering processes happen, and how energy is deposited via cluster sizes it is possible to plot cluster size against track length. This results in a plot that will show the Bragg Peak. As stated in the previous chapter, the active layers of the detector may have dead channels and chips. This is not very problematic for the high energy physics conducted at CERN as particles and showers are expected to pass through the detector. For proton CT applications on the other hand, this can have a large effect on the quality of the data. Naturally it becomes harder to track particles if there is a missing layer. Especially if the missing layer happen to coincide with the Bragg peak position. The following three plots (6.4.7, 6.4.8, and 6.4.9) all show clear tendencies of a Bragg Peak. The coulor palette indicates the number of particles that have made it through the data filtering that is done to improve the plot. In order for a track to be used in the plot it needs to be longer than 90% of the average track length and it needs to belong to chip 0 or 1 as they have the most optimal response (figure 6.4.4 and 6.4.5). It is also possible to see the Landau distribution in response for the different layers in these plots.

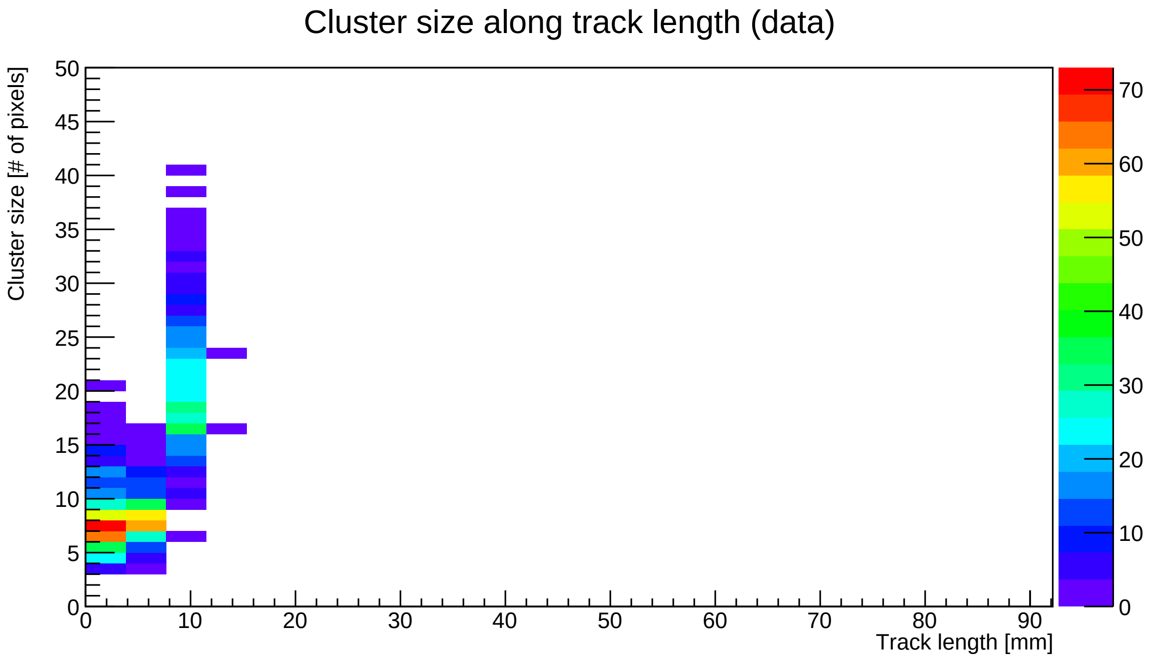

Figure 6.4.7: Sum of all runs at 122 MeV

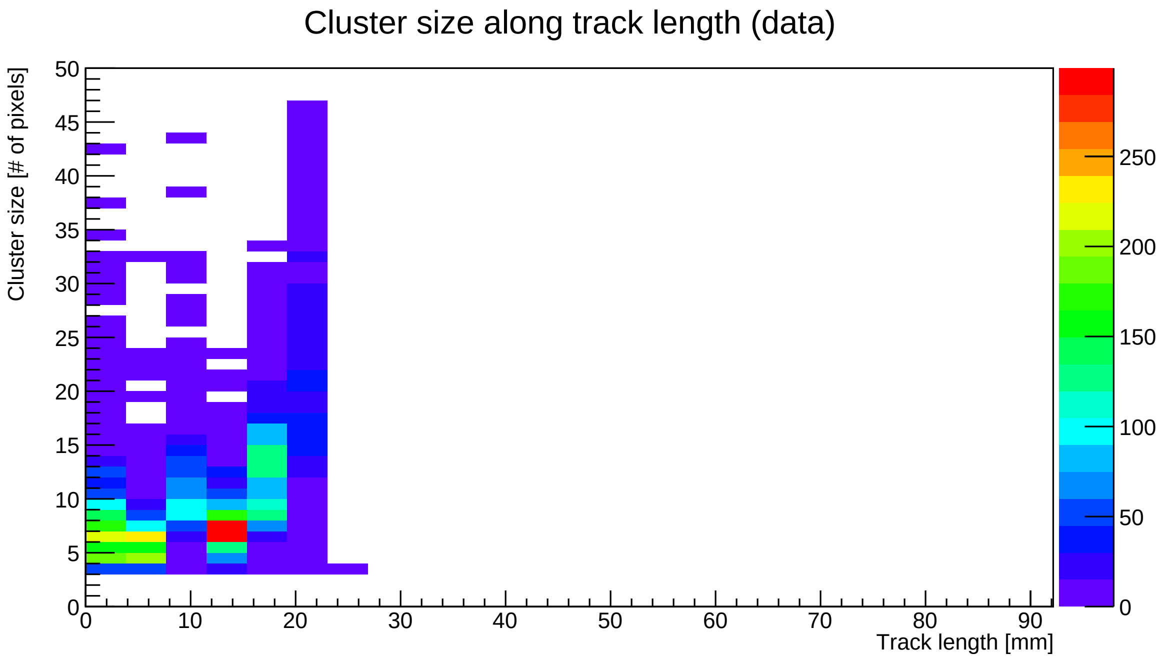

Figure 6.4.8: Sum of all runs at 170 MeV

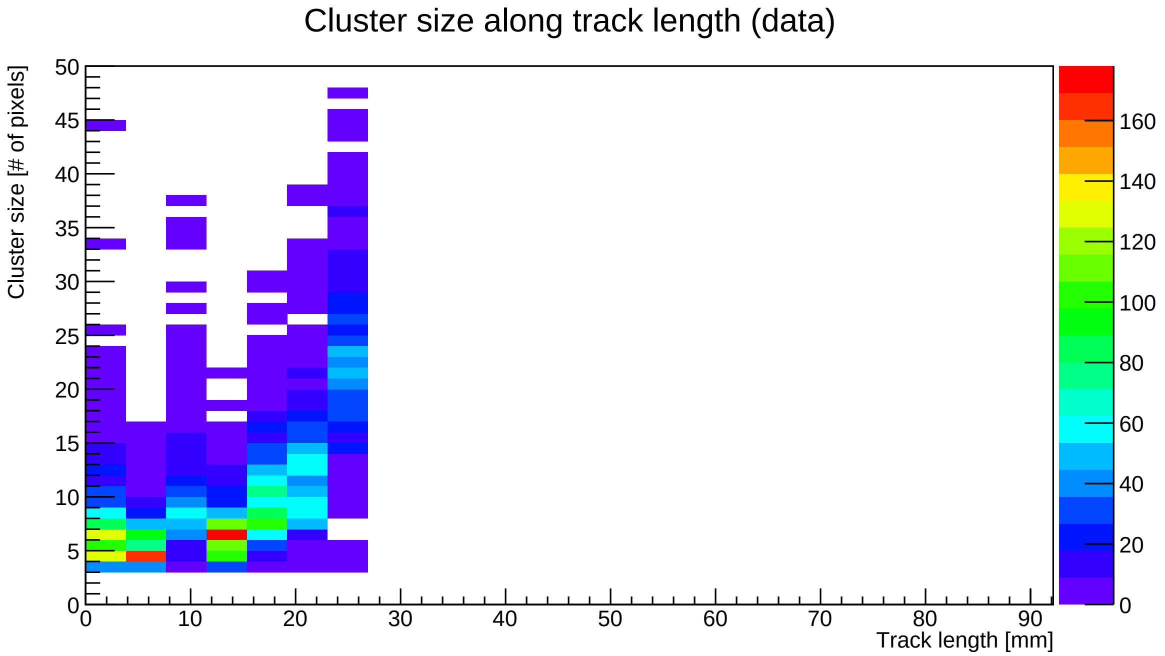

Figure 6.4.9: Sum of all runs at 190 MeV.

6.5 Range Resolution

To get good information about the density distribution of the patient one needs to get a good measurement of the energy deposited in the patient. Estimating the particle energy based on the detector response would be inacurate due to large fluctuations in the energy deposition in the sensitive layers. The large fluctuations in energy deposition also makes it problematic to only look at the total path length of a particle by following its track through the detector. A more accurate way to determine the particle range in the detector would be to reconstruct the Bragg Peak by looking at both how the energy deposition develops along the track and the total track length [1]. The reasoning for this is because if you only follow track length, then you will lose the signal at an absorber and you have no idea about how far in the track goes, only that the track stops somewhere in the absorber between to active layers. By also looking at energy deposition so that it is possible to recontruct the Bragg peak, you can more easily see if the particle will stop close to an active layer. And since the shape of the Bragg peak is known, it should be possible to reconstruct it and estimate the particle range.

In order to get a good approximation of the Bragg peak position we need to be even more selective with the tracks than before. The cluster size of the largest cluster needs to be above 22 and the ratio between the largest cluster and the previous hit needs to be at least 1.5. When the suitable tracks have been selected, the script then does a center of gravity fit between the two last hits. The result of this CoG calculation is then treated as the Bragg peak point. This estimation is probably on the lower side, but it should give a reasonably good estimate within the bounds of the detector. At last a Gauss fit is applied to the main cluster of Bragg peak points which then gives us the mean track depth of the Bragg peak and the standard deviation.

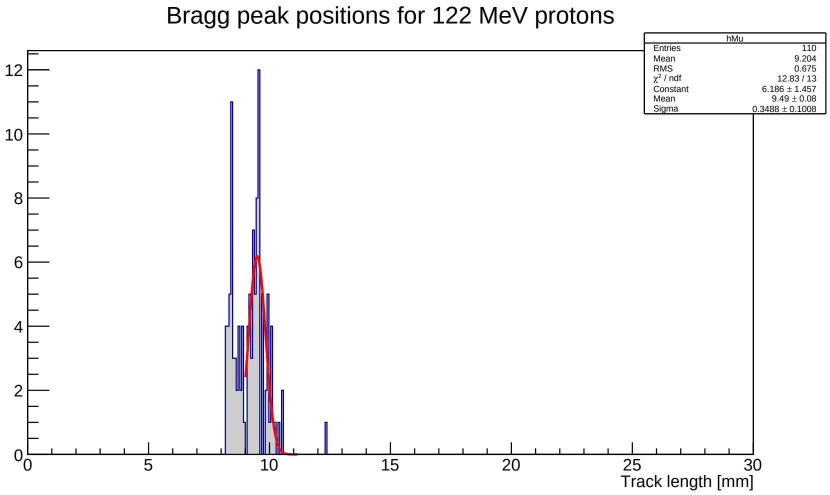

Figure 6.5.1: Estimation of Bragg peak position for 122 MeV protons.

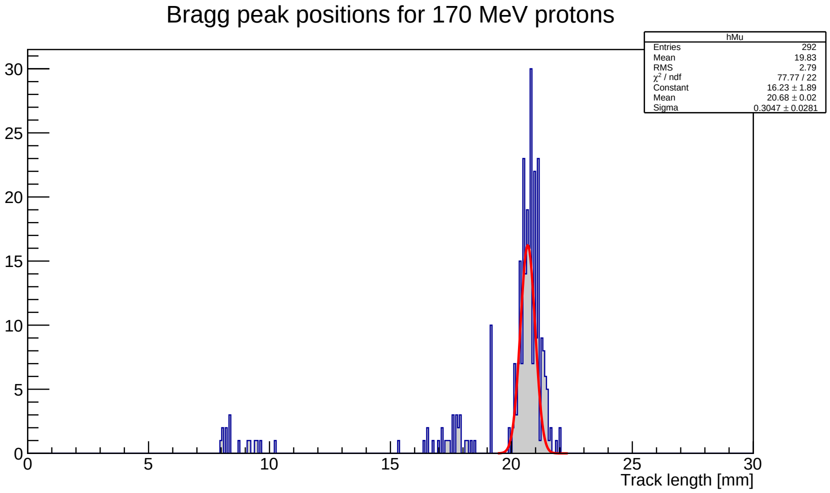

Figure 6.5.2: Estimation of Bragg peak position for 170 MeV protons.

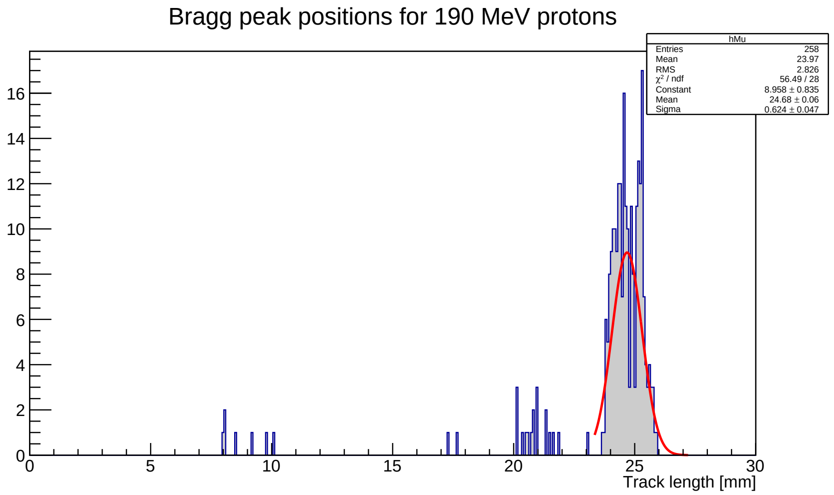

Figure 6.5.3: Estimation of Bragg peak position for 190 MeV protons

7 Conclusion

In this thesis we have looked at how the FoCal prototype, a very high granularity digital calorimeter, has performed in a proton beam at therapeutical energies with thoughts on how it can perform in proton CT. One of the main concerns in proton CT is to determine the range of the protons in the detector as it is possible to infer the incoming energy based on the range. By determining the energy of the incident protons, one can find out how much energy was lost in the patient and then calculate the stopping power in the patient. This will allow for a precise calculation of dose distribution during radiation treatment.

The particle range was determined by locating the Bragg peak in the detector. We started out by reconstructing the proton tracks. This was done by locating pixel clusters in the sampling layers of the detector and then reconstructing tracks by picking the best candidates in subsequent layers. Once the tracks had been found it was possible to measure how far the protons had travelled between sampling layers which gave us the total measurable track length. It also let us record track length vs cluster size in the sampling layers. The Bragg peak was found by filtering out tracks that were either bad because they traversed dead chips and channels or they had undergone more than average energy transfer so that their track length was too small. There was also placed lower limits on the cluster size of the last layer and the ratio in cluster size between the second-to-last and the last layers. A center of gravity calculation of the Bragg peak position was then done for the last to interaction points of a track. This will be a low end estimate, but it should be possible to reconstruct the Bragg Peak from there. With range resolution given by σ_R / R then we get the following results:

Energy [MeV]	Bragg peak position [mm]	Standard deviation [mm]	Relative Resolution
190	24.68	0.062 ± 0.047	0.025 ± 0.002
170	20.68	0.3047 ± 0.028	0.015 ± 0.001
122	9.49	0.3488 ± 0.1008	0.04 ± 0.01

References

[1] D. Aadnevik. Extremely high-granularity digital tracking calorimeter for the detection of scattered protons in proton computed tomography. Master's thesis, University of Bergen, 2014.

[2] A. Aposolou. Data analysis from the beam test at desy for the focal prototype. Master's thesis, University of Utrecht, 2013.

[3] P Blenkers. The development of a geant based monte carlo simulation framework for the r&d process of the focal calorimeter. 2012.

[4] Herman Cember and Thomas Johnson. *Introduction to Health Physics, Fourth Edition*. McGraw-Hill, 2009.

[5] Simon R Cherry, James A Sorenson, and Michael E Phelps. *Physics in nuclear medicine*. Elsevier Health Sciences, 2012.

[6] ALICE collaboration, T Peitzmann, et al. Prototype studies for a forward em calorimeter in alice. *arXiv preprint arXiv:1308.2585*, 2013.

[7] MMA Dietze. Performance study of the focal prototype detector using a 2.0-5.4 gev pure positron beam. 2014.

[8] K.A. Olive et al. Particle data group - passage of particles through matter, 2014 review. In *Particle Data Group Review*.

[9] Lee W Goldman. Principles of ct and ct technology. *Journal of nuclear medicine technology*, 35(3):115–128, 2007.

[10] Claus Grupen and Boris Shwartz. *Particle detectors*, volume 26. Cambridge university press, 2008.

[11] Ernest M Henley and Alejandro Garcia. *Subatomic physics*, volume 35. World Scientific, 2007.

[12] William R Leo. *Techniques for nuclear and particle physics experiments: a how-to approach*. Springer, 1987.

[13] Claude Leroy and Pier-Giorgio Rancoita. *Principles of radiation interaction in matter and detection*, volume 2. World Scientific, 2009.

[14] Sverre Levernes. Radiotherapy in norway. general trends 2001-2010. Technical report, Statens Straalevern, Oesteraas (Norway), 2012.

[15] Lukasz Maczewski. Measurements and simulations of maps (monolithic active pixel sensors) response to charged particles-a study towards a vertex detector at the ilc. *arXiv preprint arXiv:1005.3710*, 2010.

[16] EB Podgorsak et al. Radiation oncology physics. *a handbook for teachers and students/EB Podgorsak.–Vienna: International Atomic Energy Agency*, 657, 2005.

[17] B Schaffner and E Pedroni. The precision of proton range calculations in proton radiotherapy treatment planning: experimental verification of the relation between ct-hu and proton stopping power. *Physics in medicine and biology*, 43(6):1579, 1998.

[18] Daniela Schulz-Ertner and Hirohiko Tsujii. Particle radiation therapy using proton and heavier ion beams. *Journal of clinical oncology*, 25(8):953–964, 2007.

[19] M. Šuljic. Characterisation of monolithic active pixel sensors for the upgrade of the alice inner tracking system detector. Master's thesis, University of Trieste, 2012-13.

[20] T.F. Thorsteinsen. *Kompendium i Strålingsfysikk*. Fysisk Institutt - Universitetet i Bergen, 1995.

[21] Website:. http://www.erdit.eu/content/hadron-therapy, •.

[22] www.agorfirm.nl. Agorfirm, 2015.

[23] Kristian Ytre-Hauge. *Measurements and Monte Carlo simulations of neutron doses from radiation therapy with photons, protons and carbon ions*. PhD thesis, PhD dissertation. University of Bergen, 2013.